Earth Planet. Sci. Lett. 690 (2026) 120101

Contents lists available at ScienceDirect

Earth and Planetary Science Letters

journal homepage: www.elsevier.com/locate/epsl

Astronomical pacing of the Ludfordian Biogeochemical event, the largest carbon cycle perturbation of the Phanerozoic

Michiel Arts[a,*], Damien Pas[a,b], Jiří Frýda[c,d], Anne-Christine Da Silva[a]

[a] SediCClim Lab, Department of Geology, University of Liege, Allee du Six Aout 12, B20, 4000, Liege, Belgium
[b] Institute of Earth Sciences (ISTE), University of Lausanne, Lausanne, Switzerland
[c] Faculty of Environmental Sciences, Czech University of Life Sciences, Prague, Czech Republic
[d] Czech Geological Survey, Prague 1, Czech Republic

ARTICLE INFO

Editor: Dr. Kurt Konhauser

Keywords:
Ludfordian Biogeochemical event
Astrochronology
Carbon cycle dynamics
Ocean circulation switches

ABSTRACT

The Kosov quarry section (Prague Basin, Czech Republic) preserves one of the most complete Silurian successions spanning the Ludfordian (late Silurian) Biogeochemical Event (LBE), encompassing the mid-Ludfordian Carbon Isotope Excursion (MLCIE), the largest positive $\delta^{13}C_{carb}$ excursion of the Phanerozoic. The LBE is associated with enhanced organic carbon burial, CO_2 drawdown, redox reorganisation, climatic cooling, sea-level change, and faunal turnover, yet its tempo and driving mechanisms remain poorly constrained. Here, we establish an anchored astrochronology for the Kosov section, based on lithological induration patterns and on the estimated absolute age of the Ludfordian-Pridoli boundary. The resulting age model resolves astronomical cycles from precession to the 405-kyr eccentricity cycle, allowing us to constrain the onset of the LBE to 424.30 ± 0.61 Ma and to determine its total duration as 1.15 ± 0.26 Myr. Spectral and phase analyses reveal a strong imprint of eccentricity cycles in both the induration record and the $\delta^{13}C_{carb}$ rate-of-change record, with the latter reaching up to +0.09 ‰/kyr. The observed phase relationship indicates that the highest rates of carbon burial were synchronised with minima in astronomical eccentricity. The unusually high $\delta^{13}C_{carb}$ rates of change reflect a fundamental threshold in ocean circulation, triggered at the onset of the LBE, which reorganised the global ocean overturning system and resulted in the formation of a quasi-stable carbon reservoir that was paced by astronomical forcing. Our astrochronology thus provides the first high-resolution temporal calibration of the entire LBE and establishes a robust quantitative framework for assessing the sensitivity, pacing, and magnitude of carbon-cycle instability of Silurian $\delta^{13}C_{carb}$ excursions.

1. Introduction

Understanding large-scale carbon cycle perturbations is crucial, as they provide insights into the feedbacks that govern Earth's climate system and the thresholds beyond which these feedbacks can drive nonlinear climate responses (Berner, 2004; Gregory et al., 2009; Zeebe and Ridgwell, 2011; Isson et al., 2020). These feedbacks are mediated through changes in carbon partitioning among the atmosphere, ocean, and biosphere, which directly regulate global temperature, ocean chemistry, and redox structure. As a result, carbon redistribution influences both the onset of environmental collapse and its recovery (Cramer and Jarvis, 2020). While tectonic and volcanic processes, alongside major evolutionary and biogeochemical shifts in organic carbon burial, dominate multimillion-year trends, on timescales of 10^3 to 10^6 years, the system is sensitive to astronomical forcing (Calvert and Pedersen, 1982; Hinnov, 2018; Laurin et al., 2015; Laurin et al., 2017).

Astronomical theory posits that cyclic variations in the Earth's astronomical parameters (eccentricity, obliquity, and precession) alter the distribution and intensity of solar radiation received at the surface, leading to periodic changes in climate and oceanographic circulation (Hays et al., 1976; Hinnov and Hilgen, 2012). The global carbon cycle can respond to astronomical forcing through shifts in weathering, nutrient delivery, primary productivity, and the preservation of organic carbon in sediments (De Vleeschouwer et al., 2020; Ma et al., 2011; Vervoort et al., 2024). Although astronomical forcing's imprint on carbon burial and geochemical redox cycles is well-documented (Gambacorta et al., 2016; Huang et al., 2021; Laurin et al., 2015), its strength and expression across Pre-Cenozoic biogeochemical events

* Corresponding author.
E-mail address: michiel.arts@uliege.be (M. Arts).

https://doi.org/10.1016/j.epsl.2026.120101
Received 8 January 2026; Received in revised form 6 April 2026; Accepted 11 May 2026
Available online 4 June 2026
0012-821X/

remain poorly resolved (De Vleeschouwer et al., 2024).

The Silurian period is marked by recurrent environmental instabilities and accompanying extinctions-recovery cycles (Calner, 2008; Melchin et al., 2020; Štorch, 1995), accompanied by some of the largest $\delta^{13}C$ excursions of the Phanerozoic (Cramer and Jarvis, 2020; Claussen et al., 2024; Melchin et al., 2020; Saltzman, 2005). Notably, extinction rates were comparatively modest, implying an unusual coupling among climate, ocean circulation, the carbon cycle, and life during Silurian events (Calner, 2008; Li et al., 2021).

A longstanding paradox in Silurian stratigraphy is that many positive $\delta^{13}C$ excursions coincide with a shift toward reefal and carbonate platform facies, rather than the widespread organic-rich anoxic shale deposits typically observed during similar events in other parts of the Phanerozoic (Aldridge et al., 1993; Becker et al., 2020; Cramer and Saltzman, 2007a, 2007b; Emeis and Weissert, 2009; Jeppsso, 1990; Jeppsson et al., 1995; Munnecke et al., 2003; Ohkouchi et al., 2015). To reconcile this mismatch between large amplitude isotopic excursions and the geological record, several conceptual models have been developed. The earliest and most influential is the Primo Secundo (P-S) state model and its subsequent adaptations (Bickert et al., 1997; Cramer, 2007a, 2007b; Jeppsson, 1990; Munnecke et al., 2010), which posits that the Silurian climate and ocean circulation oscillated between two distinct modes. The P-state represents a humid, low $\delta^{13}C$ interval characterised by enhanced continental runoff and intensified hydrological cycling. These conditions promoted widespread marl deposition, while ocean circulation drove an influx of $\delta^{13}C$-depleted deep waters onto the shelf. In contrast, the S-state represents an arid, high-$\delta^{13}C$ interval characterised by reduced runoff and weakened continental weathering. This state was defined by a sluggish, salinity-driven ocean circulation that resulted in clear, oligotrophic shallow waters, which in turn drove the expansion of carbonate platforms and reef growth. Simultaneously, this reorganisation of ocean circulation led to a stratified ocean that favoured the formation of deep-ocean anoxia. Transitions from the P-state to the S-state are proposed to act as a nonlinear amplifying mechanism for Silurian $\delta^{13}C$ excursions, where the spread of deep ocean anoxia allowed for the significant burial of organic carbon required to drive Silurian $\delta^{13}C$ excursions (Bickert et al., 1997; Cramer, 2007a, 2007b; Jeppsson, 1990; Munnecke et al., 2010).

In contrast to this low-latitude–centred P-S state framework, recent Earth system modelling of the Hirnantian (latest Ordovician) shows that, at higher latitudes, Palaeozoic ocean circulation was particularly sensitive to atmospheric pCO_2 (Pohl et al., 2021). In the simulation of Pohl et al. (2021), progressive cooling driven by declining pCO_2 acts as a primary control on the oxygenation state of the deep ocean. Initial cooling suppresses high-latitude deep-water formation, leading to sluggish circulation and a decoupling between the shallow, oxygenated ocean and the deep, anoxic ocean.

Despite these different processes, both the P-S state model and the simulations of Pohl et al. (2021) converge on a similar oceanographic outcome: a decoupling between the shallow, oxygenated ocean and the deep, anoxic ocean. This stratification likely fostered a quasi-stable, anoxic deep-ocean carbon reservoir, with astronomical forcing pacing the storage and release of carbon from it. While originally proposed for the Cretaceous by Laurin et al. (2017), the concept of quasi-stable reservoirs has more recently been used to explain Silurian carbon-cycle dynamics (Sproson, 2020; Sproson et al., 2022). Both the P-S state model and the Hirnantian simulations remain largely conceptual or low-resolution, with poorly constrained temporal relationships to sea level, temperature, and astronomical forcing, compounded by the low precision of the Silurian timescale (Melchin et al., 2020). As a result, the pacing, rates, and amplification mechanisms of Silurian carbon-cycle perturbations remain unresolved, highlighting the need for integrative stratigraphic, geochemical, and astrochronological approaches.

The Ludfordian Biogeochemical Event (LBE) represents the most extreme carbon-cycle disruption of the entire Phanerozoic, culminating in the mid-Ludfordian Carbon Isotope Excursion (MLCIE), reaching $\delta^{13}C_{carb}$ values of +8-12‰ (Cramer and Jarvis, 2020). The LBE was accompanied by an extinction event, temperature and sea-level changes, and redox fluctuations (Calner, 2005; Calner and Eriksson, 2006; Calner, 2008; del Rey et al., 2023; Frýda and Manda, 2013; Frýda et al., 2021a; Kozłowski and Sobień, 2012; Trotter et al., 2016; Sproson, 2020; Zhang et al., 2022). This makes the LBE a critical test case for evaluating climate models, particularly the impact of astronomically paced climate forcing on large-amplitude $\delta^{13}C$ excursions. Despite its global expression and conceptual importance, the duration, tempo, and internal structure of the LBE remain poorly constrained. Resolving whether the LBE represents a short- or long-lived perturbation, and whether proposed climatic transitions were abrupt, gradual, or astronomically paced, requires a robust astrochronological framework capable of quantifying rates of environmental and carbon-cycle change. Specifically, high-resolution rate-of-change analysis is needed to decode the astronomical pacing of the carbon cycle and to test whether decoupling between the shallow and deep oceans could have led to the formation of a quasi-stable deep-ocean anoxia sensu Sproson (2020). By tracking how carbon isotopic shifts respond to astronomical cycles, it will become possible to determine whether such a reservoir was present during the LBE.

Here, we conduct a high-resolution cyclostratigraphic analysis of the Kosov section, which provides a near continuous sedimentary archive across the LBE. We use the induration record of Frýda et al. (2021a) as the primary proxy for astrochronological tuning, thereby enabling the estimation of durations and associated uncertainties for the LBE and its subintervals. Based on the age model of the tuned induration record, we calculate rates of change in the $\delta^{13}C_{carb}$ record (‰/kyr). We then evaluate the astronomical imprint and phasing using lithological and geochemical proxies to constrain the pacing of carbon burial and remineralisation, helping us delineate the role of astronomical forcing in pacing the carbon cycle during the LBE.

2. Geological setting

This study focuses on the upper Silurian (Ludfordian) succession at the Kosov Quarry in the Prague Basin of the Czech Republic (Fig. 1A-B). The basin forms part of the Barrandian (Teplá-Barrandian terrane) within the Bohemian Massif (Frýda and Manda, 2013; Frýda et al., 2021a, 2021b). During the Ludfordian, the terrane was situated at ~25-30°S (Scotese, 2021; Tasáryová et al., 2014), and sedimentation occurred in a deep-marine setting within an intra-plate linear rift basin subdivided into several sub-basins (Horný, 1955; Kříž, 1991). Deposition took place within a slope-to-basin system developed along the margins of the Kosov volcanic centre (Lehnert et al., 2007a; Frýda and Manda, 2013).

The studied Kosov section (No. JF195; 49°56′12.2″N, 14°03′20.1″E) provides one of the most complete records of the Ludfordian Biogeochemical Event (LBE), including the Lau/Kozlowskii Bioevent (LKB) (culmination of the Siluricus Ocean Anoxic Event, Frýda et al., (2021b)), the mid-Ludfordian Carbon Isotope Excursion (MLCIE), and a mid-Ludfordian glaciation, which together represent key components of the LBE (Lehnert et al., 2007b; Frýda et al., 2021a, 2021b; Frýda and Manda, 2013) (Fig. 1B). The locality has been extensively investigated with studies documenting sedimentological, palaeontological, geochemical, and faunal changes across the LBE (del Rey et al., 2023; Farkaš et al., 2016, 2024; Frýda et al., 2021a, 2021b; Frýda and Manda, 2013; Kříž, 1992; Manda and Kříž, 2006; Štorch, 1995; Tonarová et al., 2025; Zhang et al., 2022) (Fig. 1).

The Ludfordian succession exposed at Kosov Quarry belongs to the upper Kopanina Formation (Kříž, 1992; Lehnert et al., 2007a) (Fig. 2A). The section begins with dark brown to grey finely laminated shales that rapidly transition into interbedded limestone beds (Horný, 1955; Kříž, 1991; Lehnert et al., 2007a; Frýda and Manda, 2013; Gocke et al., 2012; Mergl and Frýda, 2025). In the lower part of the section, limestone beds are interbedded with shales, while in the middle and upper

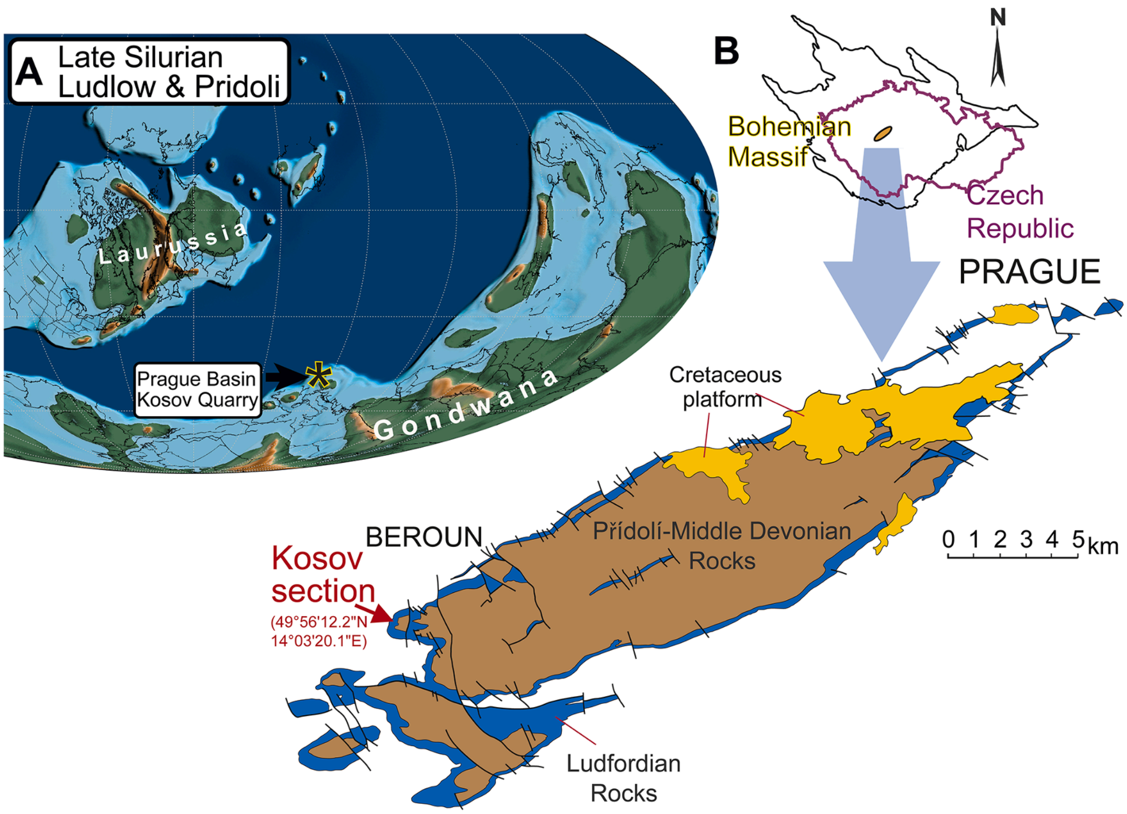

Fig. 1. Overview of the Kosov section. A. Location of the Kosov quarry section in a Late Silurian (420 Ma) (modified after Scotese, 2021). B. Location of the Kosov section in the Silurian strata of the Prague syncline in the Czech Republic (modified after Frýda et al., 2021a).

parts they are interbedded with marls, forming laterally continuous limestone-marl/shale couplets that characterise the deeper-water facies of the upper Kopanina Formation (Lehnert et al., 2007a; Kříž, 1992; Manda et al., 2012; Gocke et al., 2012).

The Kosov section encompasses the mid-Ludfordian Carbon Isotope Excursion (MLCIE) of the LBE, which is subdivided into three chemostratigraphic zones: the R, S, and F Zones (Frýda and Manda, 2013) (Fig. 2E, F, H). The R-Zone marks the rapid positive shift in $\delta^{13}C_{carb}$ values after the last appearance datum of *P. siluricus* and corresponds (Frýda et al., 2021b). The S-Zone represents the high $\delta^{13}C_{carb}$ plateau, while the F-Zone is characterised by a gradual decline in $\delta^{13}C_{carb}$ values (Allman et al., 2024; Frýda et al., 2021b).

3. Materials and methods

A cyclostratigraphic analysis was performed on the induration record extracted from the litholog published by Frýda et al. (2021a). The R code and Quarto used for this analysis are available at: https://github.com/stratigraphy/Kosov-cyclostrat. The curve shown on the right-hand side of the published litholog (Fig. 2A, G) of Frýda et al. (2021a) was extracted using Adobe Illustrator and subsequently rescaled to a 0-5 induration scale, from 0 the least competent to 5 most competent.

3.1. Primary depositional analysis of the rhythmic bedding in the Kosov section

To establish a reliable cyclostratigraphic framework, it is imperative to determine whether the rhythmic bedding at the Kosov section reflects primary environmental pacing or secondary diagenetic overprinting since the origin of limestone-marl alternations is frequently debated (Munnecke et al., 2023; Westphal, 2006). Microfacies analysis shows that the limestone beds contain coarse organo-detrital components and pervasive bioturbation, whereas the interbedded shales are thinly laminated (Gocke et al., 2012). With limestone beds hosting distinct brachiopod and trilobite assemblages that differ from those in the shale interbeds (Mergl and Frýda, 2025; Vokáč, pers. comm., 2026). The presence of localised hardgrounds atop the limestone beds, colonised by epifauna, demonstrates that limestone beds attained competence on the seafloor (Frýda, unpublished observation). The $\delta^{13}C_{org}$ values in the limestone beds are consistently 2‰ lighter than those in the shales, a systematic isotopic offset not observed in diagenetic limestones (Allman et al., 2024). Furthermore, $^{87}Sr/^{86}Sr$ ratios in these limestones follow the Ludfordian seawater trend (Farkaš et al., 2016)(0.7083-0.7087), and the stability of $\delta^{34}S$ pyrite signals across both lithologies (Frýda et al., 2021a, 2021b; Allman et al., 2024) indicates that the succession has not been subjected to a high degree of post-depositional alteration (Roberts et al., 2018). Sedimentological and geochemical observations from the Kosov quarry therefore indicate that the beds are of primary origin, with varying carbonate-to-clay ratios, where higher carbonate content produces the competent beds in the observed rhythmic alternation (Pas et al., 2024; Boulila et al., 2010; Weedon, 2003). The record's bimodal distribution, characterised by strong contrasts between soft shales and limestone, likely resulted from early diagenetic CaCO migration that amplified pre-existing variability (Bathurst, 1987; Marsaglia et al., 2017; Frýda et al., 2021a). Since the litholog was generated independently of cyclostratigraphic objectives, any observational bias is minimised. Collectively, the sedimentological, paleontological, and geochemical evidence confirms that the Kosov induration record preserves a primary environmental signal suitable for cyclostratigraphic analysis.

3.2. Spectral analysis and construction of the astrochronology

The cyclostratigraphic study of the induration and the $\delta^{13}C_{carb}$ records used the WaverideR (Arts et al., 2024; Arts, 2023) and Astrochron

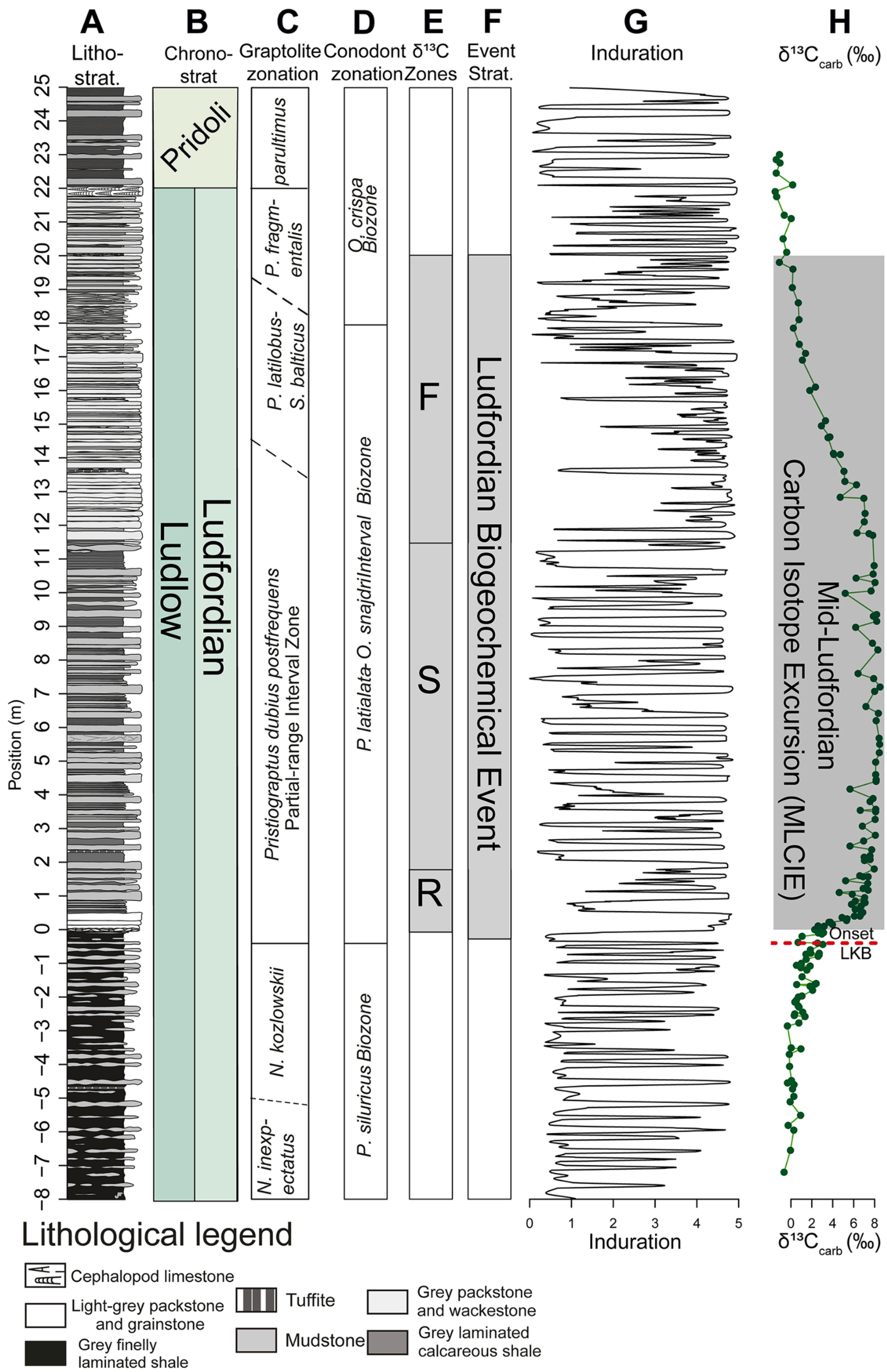

Fig. 2. Stratigraphic setting, Kosov Quarry section A. Litholog B. Chronostratigraphy C. Graptolite Zonation D. Conodont Zonation E. Carbon isotope zonation. F. Event stratigraphy. I. Induration record extracted from Fig. 2A. G. combined $\delta^{13}C_{carb}$ records of Farkaš et al. (2016) and Frýda et al. (2021a). Noted are the onset of the Lau/Kozlowskii Bioevent and the mid-Ludfordian Carbon Isotope Excursion (MLCIE) after Frýda et al. (2021b). A-H - modified after Frýda and Manda (2013), and Frýda et al. (2021a,b).

(Meyers, 2019, 2015) R packages. The cyclostratigraphic analysis began by applying the Time Optimisation (TimeOpt) function of the astrochron R package to the induration record, yielding a first-order estimate of the sedimentation rate (Meyers, 2015). The TimeOpt function was run twice: once to evaluate the 405-kyr eccentricity amplitude modulation of the 100-kyr eccentricity band and the concentration of power at the 100-kyr and 405-kyr eccentricity frequencies, and once to evaluate the same parameters at the precession and 100-kyr eccentricity frequencies. The optimal fit of the astronomical cycles was evaluated over a range of sediment accumulation rates from 0.1 to 3 cm/kyr, encompassing the minimum and maximum estimates of the duration of the studied interval (Arts et al., 2024; Cramer et al., 2015; Melchin et al., 2020).

The first-order sedimentation rate estimate from the TimeOpt runs was used to calculate the period (m) of the 405-kyr eccentricity cycle, making it possible to filter the 405-kyr eccentricity cycle from the induration record. The extracted cycle was then used for minimal tuning, in which the distance (m) between successive peaks of the cycle was used to create a period (m) curve for the 405-kyr eccentricity cycle (Hinnov, 2013). This period (m) was then used to guide the tracking of the period (m) of the 405-kyr eccentricity cycle in the continuous wavelet transform (CWT) scalogram. The tracked period (m) curve was then recalculated using the ratios between the 405-kyr eccentricity cycle and those of other known astronomical cycles. These (recalculated) curves were then overlain on the CWT scalogram to verify whether they passed through regions of high spectral power, thereby validating the presence of known astronomical cycles.

The tracked 405-kyr eccentricity period (m) curve was used to establish an anchored astrochronology by tying the floating timescale to the astrochronologically calibrated age of the Ludlow-Pridoli boundary (423.03 $\pm$ 0.53 Ma) (see Arts (2023) for the used technique and see Arts et al. (2024) for the revised age of the Ludlow-Pridoli boundary). The Ludlow-Pridoli boundary is placed at 22 m, with an uncertainty of $\pm$2 m to account for diachrony in biozonation. The anchoring modelling workflow also includes an astronomical cycle peak check that rejects modelling runs lacking spectral peaks corresponding to expected astronomical cycles. The cycle targets used for this check are 405 $\pm$ 20.25 kyr, 110 $\pm$ 35 kyr, 33 $\pm$ 7 kyr, and 19 $\pm$ 6 kyr, corresponding to expected durations of the long eccentricity, short eccentricity, obliquity, and precession cycles during the Silurian (Farhat et al., 2022; Waltham, 2015; Wu et al., 2024). The uncertainties of the targets are set conservatively to reflect the uncertainty of these astronomical cycles during the Silurian. The anchored numerical age model was then used to assign ages and durations (with uncertainties) to the Kosov section record and its subsections.

The anchored age model also enabled the study of the imprint of astronomical cycles in the induration record in the time domain. Special attention was paid to the phase relationship between the 100-kyr eccentricity cycle directly extracted from the record and the 100-kyr eccentricity cycle extracted from the Hilbert transform of the precession cycle, and between the 405-kyr eccentricity cycle directly extracted from the record and the 405-kyr eccentricity cycle extracted from the Hilbert transform of the 100-kyr eccentricity cycle. The phase relationship between these cycles allowed inference of the cycle's phases extracted from the proxy record relative to the true phases of the astronomical cycles (Hinnov, 2000; Laskar et al., 2004). The combined $\delta^{13}C_{carb}$ records of Farkaš et al. (2016) and Frýda et al. (2021a) were also converted to the time domain, enabling the calculation of the rate of change (‰/kyr) of the tuned $\delta^{13}C_{carb}$ record. This record was subsequently investigated for imprint of astronomical cycles.

4. Results

4.1. Building an age model for the Ludfordian Biogeochemical event

The TimeOpt consistently identifies an optimal sedimentation rate centred at approximately 1.8 cm/kyr, with a broader interval of elevated fits between 1.2 and 2.0 cm/kyr (Fig. 3A, B, E, F). In the TimeOpt run evaluating the 405-kyr eccentricity amplitude modulation of the 100-kyr eccentricity band, together with the concentration of spectral power at the 405-kyr and 100-kyr eccentricity frequencies, both the envelope fit (r^2[envelope]) and the combined optimal fit metric (r^2[opt]) converge toward a pronounced maximum near 1.8 cm/kyr. In contrast, the r^2 power spectrum metric displays a less sharp response (Fig. 3A, B). At the optimal solution of 1.8 cm/kyr, the reconstructed eccentricity model closely tracks the amplitude envelope of the filtered short eccentricity signal, indicating coherent eccentricity-driven amplitude modulation (Fig. 3C, D). In the second TimeOpt run, evaluating the eccentricity amplitude modulation of the precession band and the concentration of power at the precession and 100-kyr eccentricity frequencies, the overall fit of values is lower. Nevertheless, both r^2[envelope] and r^2[opt] again converge toward a maximum at approximately 1.8 cm/kyr, while the r^2 power spectrum is more ambiguous (Fig. 3E, F). At the corresponding optimal solution of 1.8 cm/kyr, the reconstructed eccentricity model follows the amplitude envelope of the filtered precession signal, but with reduced coherence relative to the other modelling run (Fig. 3C, D, G, H).

Based on the sedimentation rate estimates obtained from the TimeOpt modelling run, the 405-kyr eccentricity cycle was extracted from the induration record using a Taner band-pass filter spanning 4.86-8.1 m (Fig. 4A). When superimposed on the original signal, the filtered 405-kyr cycle appears as a primary modulating rhythm of intervals with low and high induration values (Fig. 4A). Next, a sedimentation-rate curve was constructed using the minimal-tuning technique, in which the distance between successive peaks of the extracted cycle is set to the duration of the interpreted astronomical cycle yielding a varying sedimentation-rate (cm/kyr) curve (Fig. 4B).

The sedimentation rate curve (cm/kyr) obtained from the minimal tuning was multiplied by 4.05 to get the corresponding period (m) curve of the 405-kyr eccentricity cycle (Fig. 5). This period (m) curve was then superimposed on the CWT scalogram (Fig. 5), where the curve can be observed to pass through an area of high spectral power, verifying with the presence of the 405-kyr eccentricity cycle in the induration record. Next, the period (m) of the 405-kyr cycle was tracked within the CWT (shown as the grey line in Fig. 5). To test the validity of this tracked period (m) curve, it was rescaled using the ratios between the 405-kyr eccentricity cycle and the 100-kyr eccentricity, obliquity, and precession cycles (Laskar et al., 2004, 2011; Waltham, 2015). The recalculated period curves for 100-kyr eccentricity, obliquity, and precession validate the original 405-kyr CWT, as they pass through regions of high spectral power. However, as the power of these shorter cycles is intermittent and noisy, their interpretation requires caution.

The tracked period (m) curve of the 405-kyr eccentricity cycle was used to construct a floating astrochronology, with an assigned uncertainty based on the analytical uncertainty of the wavelet transform (Arts et al., 2024). This floating age model with uncertainty was then anchored to the astrochronologically calibrated age of the Ludlow-Pridoli boundary (423.03 $\pm$0.53 Ma) (Arts et al., 2024) (Fig. 6). The anchoring modelling workflow included a $\pm$2 m added uncertainty for the Ludlow-Pridoli boundary and a check for the preservation of spectral peaks of known astronomical cycles to reject unrealistic age models and constrain uncertainty propagation away from the anchoring point.

The anchored numerical age model was used to assign ages and durations (with uncertainties) to the Kosov section, its subsections and the biozones (Frýda et al., 2021b; Frýda and Manda, 2013) (Table 1). The calculated ages, durations, and uncertainties were rounded to the nearest 10 kyr to align with the precision of the anchor point (Table 1).

4.2. Proxy records and astronomical cycles in the numerical time domain

The age model was used to convert the induration and $\delta^{13}C_{carb}$ records to the numerical time domain (Fig. 7A-E). Subsequently, the CWT was applied to the tuned induration record (Fig. 7F). Fig. 7F shows spectral peaks corresponding the ~8.5 kyr (half precession?) ~16-kyr (precession), 28-kyr (obliquity), 50-kyr (eccentricity), 100-kyr (eccentricity), 200-kyr (eccentricity), 405-kyr (eccentricity) and 800-kyr (eccentricity?) cycle (Fig. 7F) (for additional EHA and MTM spectra of the tuned induration record (see SI 2.).

To further analyse these cycles, the precession, obliquity, 100-kyr eccentricity, and 405-kyr eccentricity cycles were extracted from the tuned induration record (Fig. 7F-J). When these extracted cycles are overlaid on the tuned induration record, it becomes evident that obliquity and precession form the primary bed-to-bed pattern, with the 100- and 405-kyr eccentricity cycles modulating intervals of low and high induration values. Additionally, the Hilbert transform was applied to the precession, obliquity, and 100-kyr eccentricity cycles extracted from the tuned induration record (Fig. 7H, I, K). The 100 and 405-kyr eccentricity cycles were extracted from the Hilbert transform-derived

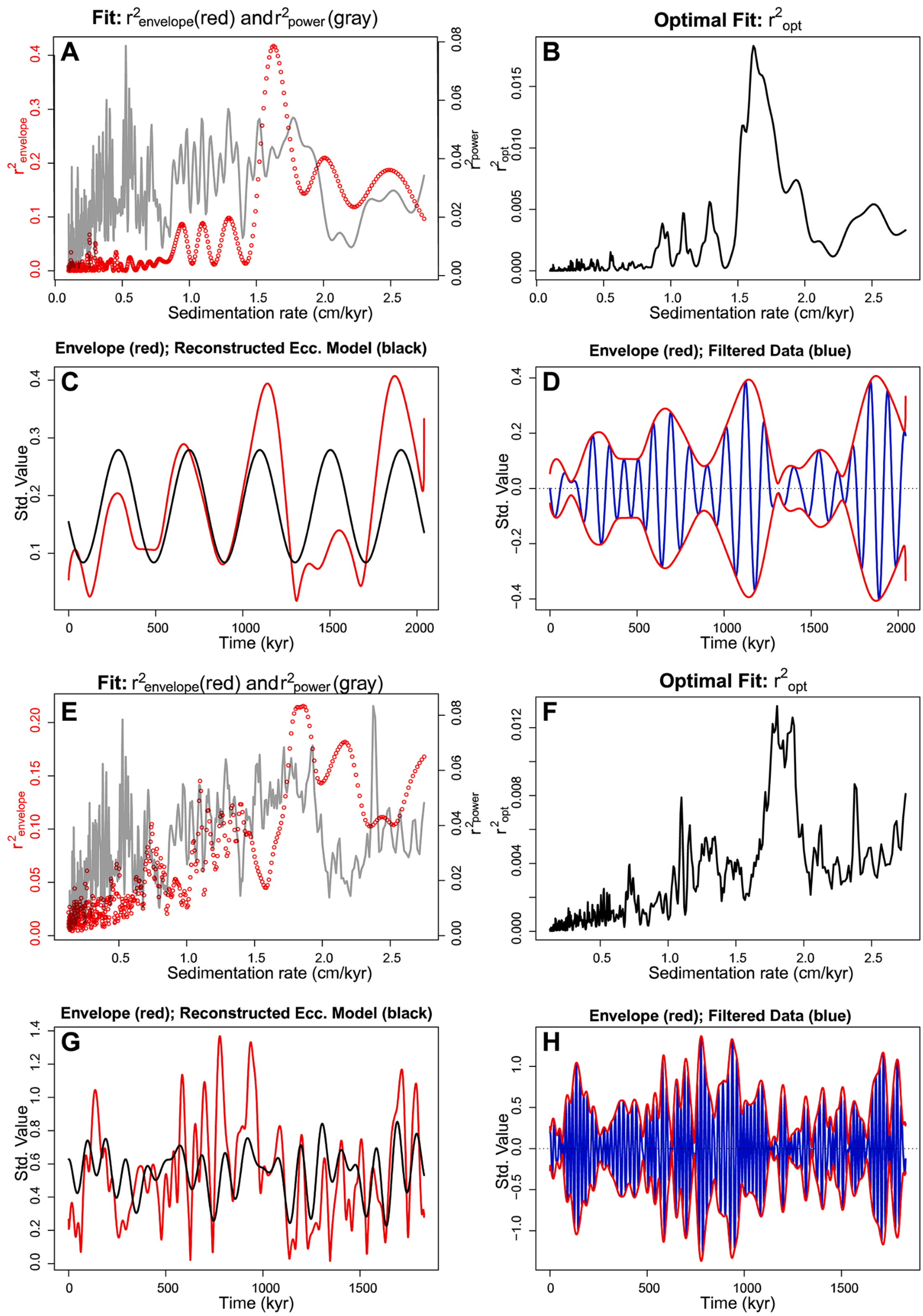

Fig. 3. TimeOpt results. A. Fit: r^2[envelope] (red) and r^2[power] (grey) for TimeOpt run 405 vs 100-kyr ecc. B. Optimal Fit: r^2[opt] for TimeOpt run 405 vs 100-kyr eccentricity. C. Envelope (red); Reconstructed eccentricity. Model (black) for TimeOpt run 405 vs 100-kyr eccentricity. D. Envelope (red); Filtered Data (blue) for TimeOpt run 405 vs 100-kyr eccentricity. E. Fit: r^2[envelope] (red) and r^2[power] (grey) for TimeOpt run 100-kyr eccentricity versus precession. F. Optimal Fit: r^2[opt] for TimeOpt run 100-kyr eccentricity versus precession. G. Envelope (red); Reconstructed eccentricity. Model (black) for TimeOpt run 100-kyr eccentricity versus precession. H. Envelope (red); Filtered Data (blue) for TimeOpt run 100-kyr eccentricity versus precession.

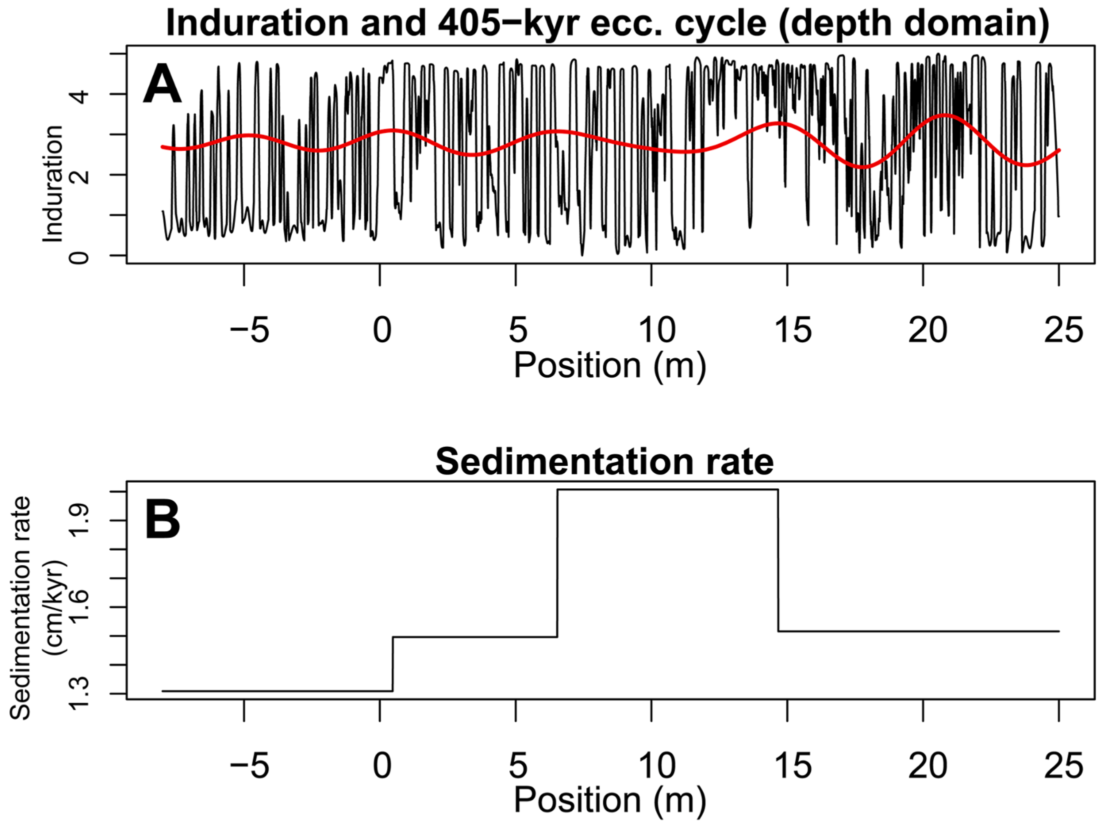

Fig. 4. Minimal tuning. A. Induration record and the extracted 405-kyr eccentricity cycle. B. Sedimentation rate (cm/kyr) based on the minimal tuning.

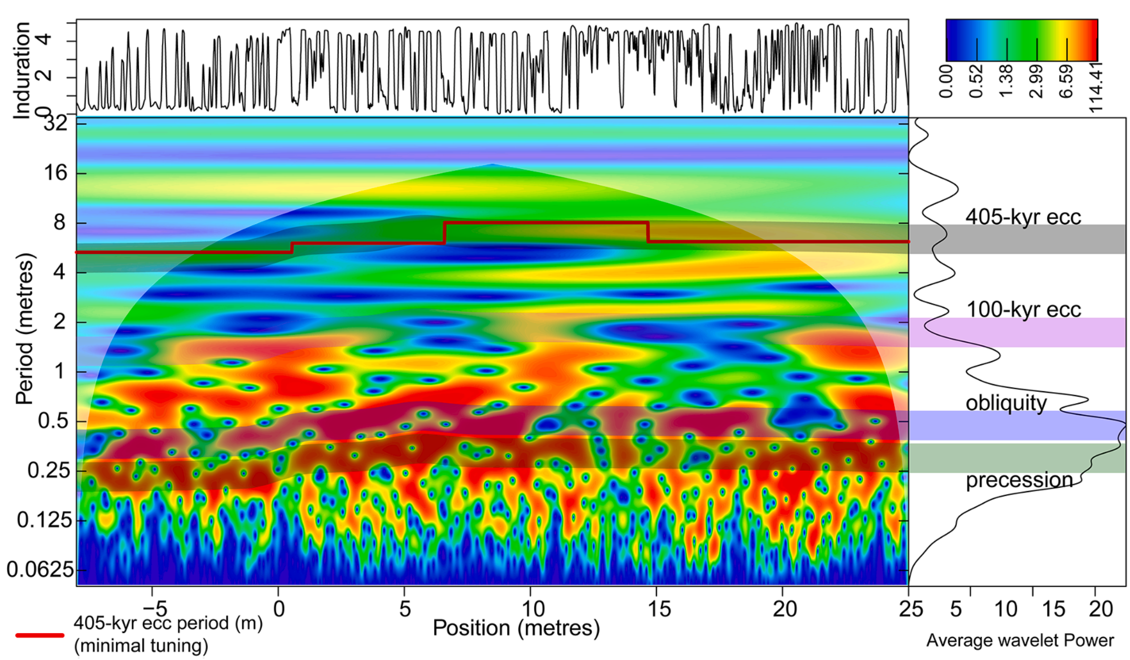

Fig. 5. The Continuous Wavelet Transform (CWT) of the induration record extracted from the litholog of Frýda et al. (2021a) and the period (m) of astronomical cycles based on the sedimentation rates attained from the minimal tuning and the tracked period (m) of the 405-kyr eccentricity cycle. Black line = tracked period (m) of the 405-kyr eccentricity cycle. Red line = the period (m) of the 405-kyr eccentricity cycle (minimal tuning based). Purple line = the 100-kyr eccentricity cycle (recalculated tracked period (m) of the 405-kyr eccentricity cycle). Blue line = the obliquity cycle (recalculated tracked period (m) of the 405-kyr eccentricity cycle). Dark green line = the precession cycle (recalculated tracked period (m) of the 405-kyr eccentricity cycle).

amplitude record of the precession and 100-kyr eccentricity cycle and compared to the 100 kyr and 405-kyr eccentricity cycles directly extracted from the record (Fig. 7H-J). Both the 100-kyr and 405-kyr eccentricity cycles extracted from the Hilbert transform amplitudes of the 100-kyr eccentricity cycle, and precession are antiphased relative to their counterparts directly extracted from the induration record

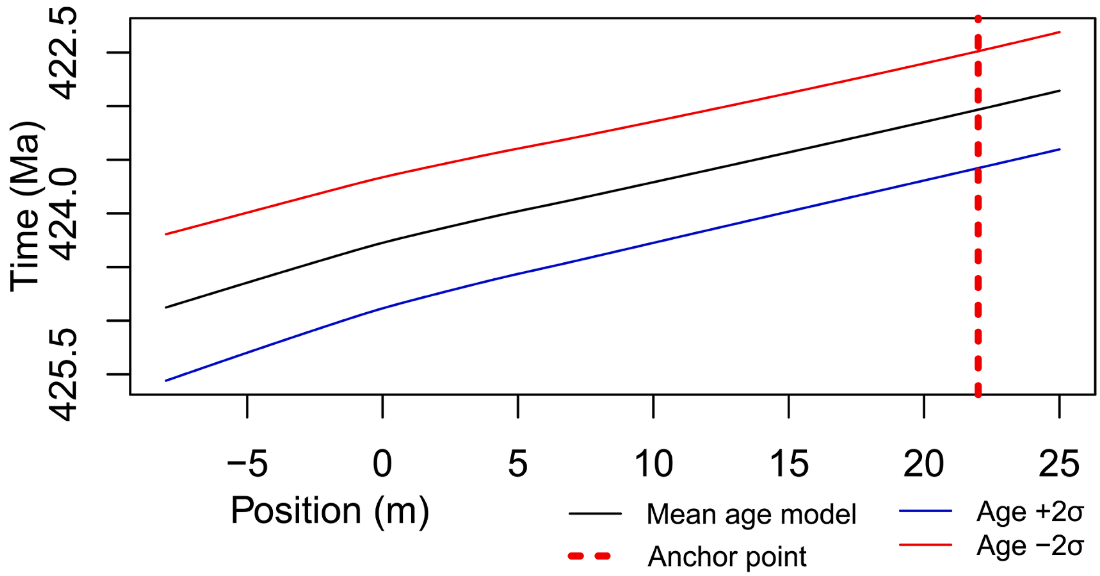

Fig. 6. Astrochronological numerical age- depth model. The black line is the mean age-depth curve, and the red and blue lines are time plus and minus two standard deviations (2σ). The red dotted line is the anchor point at the Ludfordian-Pridoli boundary at 22m.

Table 1
Durations and ages for chronostratigraphic/geochronologic units, lithological units, events and conodont zones. All dates are rounded to the nearest 10 kyr to agree with the accuracy of the anchor of the Ludfordian-Pridoli boundary.

Interval	position (m) bottom	position (m) top	Age bottom (Ma) ±2sd	Age top (Ma) ±2sd	duration (kyr) ±2sd
Entire record	-8.00	25.00	424.87 ± 0.68	422.86 ± 0.55	2020 ± 450
Ludfordian Biogeochemical Event	-0.40	20.00	424.30 ± 0.61	423.15 ± 0.55	1150 ± 260
LKB (culmination of the Siluricus Ocean Anoxic Event)	-0.40	0.00	424.30 ± 0.61	424.27 ± 0.61	30 ± 10
Elevated (Trace) metal concentrations	-4.4	0.4	424.6 ± 0.65	424.25 ± 0.61	350 ± 80
Mid-Ludfordian Carbon Isotope Excursion (MLCIE)	0.00	20.00	424.27 ± 0.61	423.15 ± 0.55	1120 ± 250
R-zone	0.00	1.40	424.27 ± 0.61	424.18 ± 0.60	90 ± 20
S-Zone	1.40	11.60	424.18 ± 0.6	423.62 ± 0.56	570 ± 130
F-Zone	11.60	20.00	423.62 ± 0.56	423.15 ± 0.55	470 ± 110
Ludlow part section	0.00	22.00	424.27 ± 0.61	423.03 ± 0.54	1240 ± 280
Pridoli part section	22.00	25.00	423.03 ± 0.54	422.86 ± 0.55	180 ± 40
P. siluricus Biozone part section	-8.00	-0.40	424.87 ± 0.68	424.3 ± 0.61	570 ± 130
P. latialata - O. snajdri Interval Biozone	-0.40	18.00	424.3 ± 0.61	423.26 ± 0.55	1040 ± 230
O. crispa Biozone part section	18.00	25.00	423.26 ± 0.55	422.86 ± 0.55	400 ± 90

(Fig. 7G, J).

4.3. $\delta^{13}C_{carb}$ (rate-of-change) curves

The rate of change (‰/kyr) of the $\delta^{13}C_{carb}$ curve was calculated from the LOWESS regression line applied to the $\delta^{13}C_{carb}$ record to minimise the influence of short-term local noise (Fig. 8E-F). The rate of change (‰/kyr) reaches a maximum of +0.09 (‰/kyr) during the onset of the LBE (Fig. 8F). The rate-of-change (‰/kyr) record shows a strong imprint of the 100-kyr eccentricity cycle, which was subsequently extracted and plotted (Fig. 8F-G). The 100-kyr eccentricity cycle extracted from the rate-of-change (‰/kyr) record is generally in phase with the 100-kyr eccentricity cycle extracted from the induration record during the LBE (Fig. 8F-G).

5. Discussion

5.1. Astrochronology and the imprint of astronomical cycles through the Ludfordian Biogeochemical Event

The establishment of the astrochronological framework for the Kosov section represents a new step toward quantifying the tempo of the LBE and completing the (Silurian) astronomical timescale. The new anchored astrochronology provides a high-resolution temporal calibration, allowing us to examine the imprint of astronomical cycles and their role in modulating processes during the LBE.

The anchored astrochronological age model was used to assign ages, durations, and associated uncertainties to chrono- and geochronologic units, lithological units, and events in the Kosov section (see Table 1). The LBE started at 424.30 ± 0.61 Ma and lasted 1150 ± 260 kyr. In contrast, the LKB (culmination of the Siluricus Ocean Anoxic Event, Frýda et al., (2021b)) lasted only 30 ± 10 kyr. A previous estimate for the onset of the LBE is based on a dated hiatus in the Cellon section, spanning 424.19 ± 0.55 Ma to 423.83 ± 0.55 Ma (Arts et al., 2024). Another age constraint is a U-Pb zircon age of 424.08 ± 0.20 Ma, from Podolia, Ukraine, from a bentonite located less than 1 m below the onset of the MLCIE (Cramer et al., 2015). The new astrochronologically tuned age for the onset of the LBE (424.30 ± 0.61) falls within the range of these published ages. The increase in uncertainty away from the anchor point was constrained in the modelling workflow by a check for the preservation of spectral peaks of known astronomical cycles, thereby rejecting outliers and reducing the increase in uncertainty away from the tie-point, resulting in a semi-objective measure of cyclostratigraphic

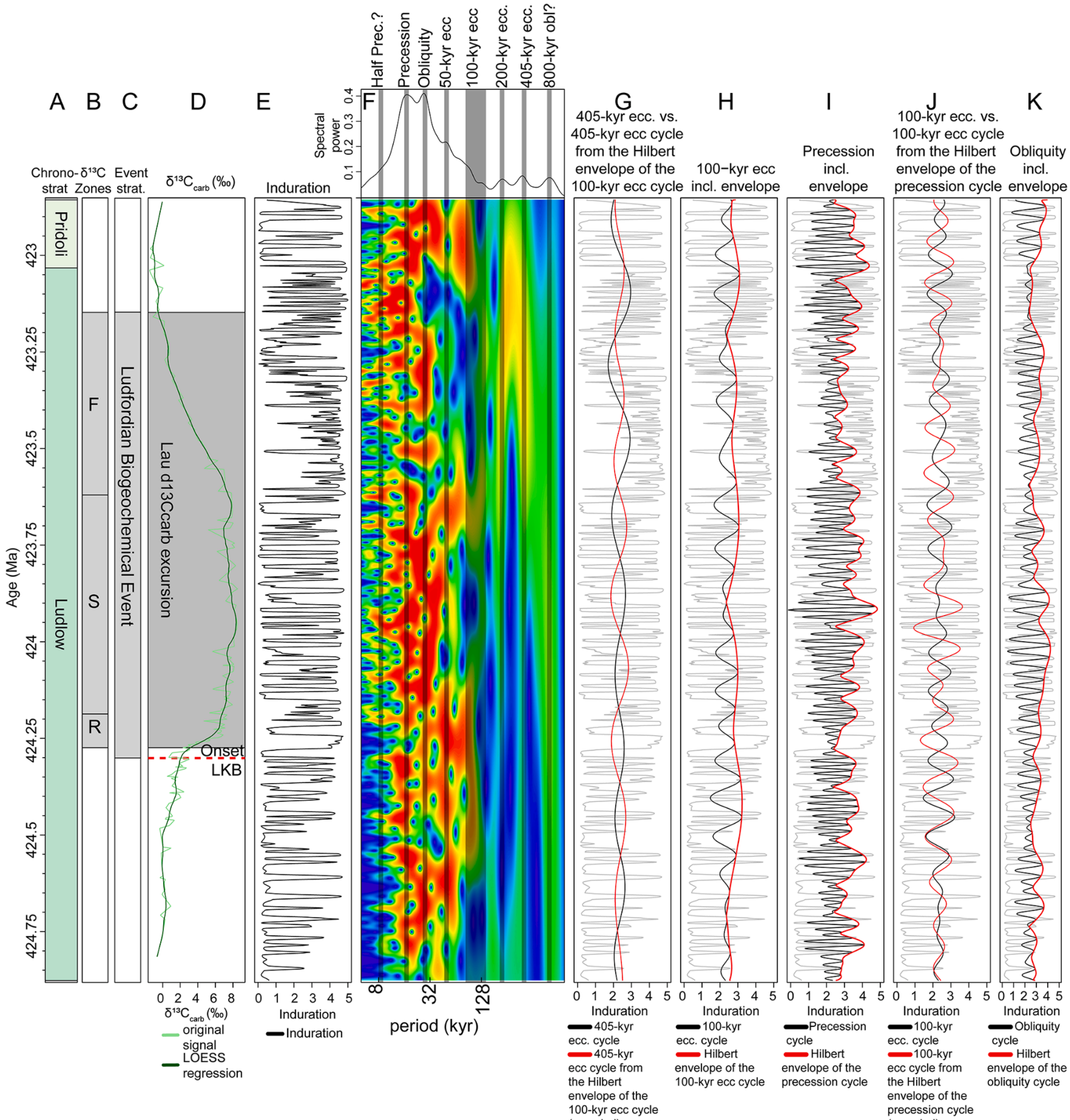

Fig. 7. Induration proxy record in the time domain, including the wavelet scalogram of the induration record and astronomical cycles extracted from said record. A Stages. B. Event zone subdivision C. Event stratigraphy. D. The $\delta^{13}C_{carb}$ record. E. The Induration record. F. Wavelet scalogram of the induration record with the average spectral power on top. The black vertical lines in the wavelet scalograms are durations of known astronomical cycles. From left to right, these cycles are the 8.5-kyr half precession, ~16-kyr precession, 28-kyr obliquity,50-kyr eccentricity, 100-kyr eccentricity, 200-kyr eccentricity and the 405-kyr eccentricity cycle. G. The black line is a 405-kyr eccentricity cycle extracted from the Induration record. The red line is the 405-kyr eccentricity cycle extracted from the Hilbert transform of the 100-kyr eccentricity cycle of the Induration record. H. The 100-kyr eccentricity cycle was extracted from the Induration record (black line) and the Hilbert transform of the 100-kyr eccentricity cycle (red line). I. Precession cycle extracted from the Induration record (black line), and the Hilbert transform of the precession cycle (red line). J. The black line is a 100-kyr eccentricity cycle extracted from the Induration record. The red line is the 100-kyr eccentricity cycle extracted from the Hilbert transform of the precession cycle of the Induration record. K. The obliquity cycle extracted from the Induration record (black line) and the Hilbert transform of the precession cycle (red line).

uncertainty, avoiding the subjectivity of cycle-error counting.

By isolating the precession, obliquity, and the 100 and 405-kyr eccentricity cycles from the tuned induration record, the hierarchical imprint of astronomical forcing becomes particularly clear (Fig. 7G-K). Bed-scale induration alternations are primarily paced by precession and obliquity, while their organisation into larger bundles is governed by eccentricity in a systematic hierarchy characteristic of astronomical forcing (Hinnov, 2000; Laskar et al., 2004; Laskar, 2020).

The periods interpreted as obliquity (28 kyr) and precession (16 kyr) cycles are at the shorter end than is expected for the Silurian (Farhat et al., 2022; Waltham, 2015; Wu et al., 2024), yet remain within the current uncertainty range for the estimated durations of these cycles during the Silurian. Obliquity and precession, but even more so the half precession, are at or even near the resolution of the record. As such, care should be taken when interpreting these cycles, as some of the extracted individual wiggles may be artefacts of signal processing. Complementary EHA and MTM-based spectral analyses do contain clear obliquity and precession peaks, while the amplitude of the half-precession peak is low, so a harmonic origin of the half-precession cycle cannot be discounted (see SI 2). Since the imprint of obliquity and precession is suboptimal, calculations of parameters such as the Earth-Moon distance were not attempted, as it would introduce an unquantified uncertainty into any estimates.

A spectral peak of ~55 kyr was observed in the average CWT

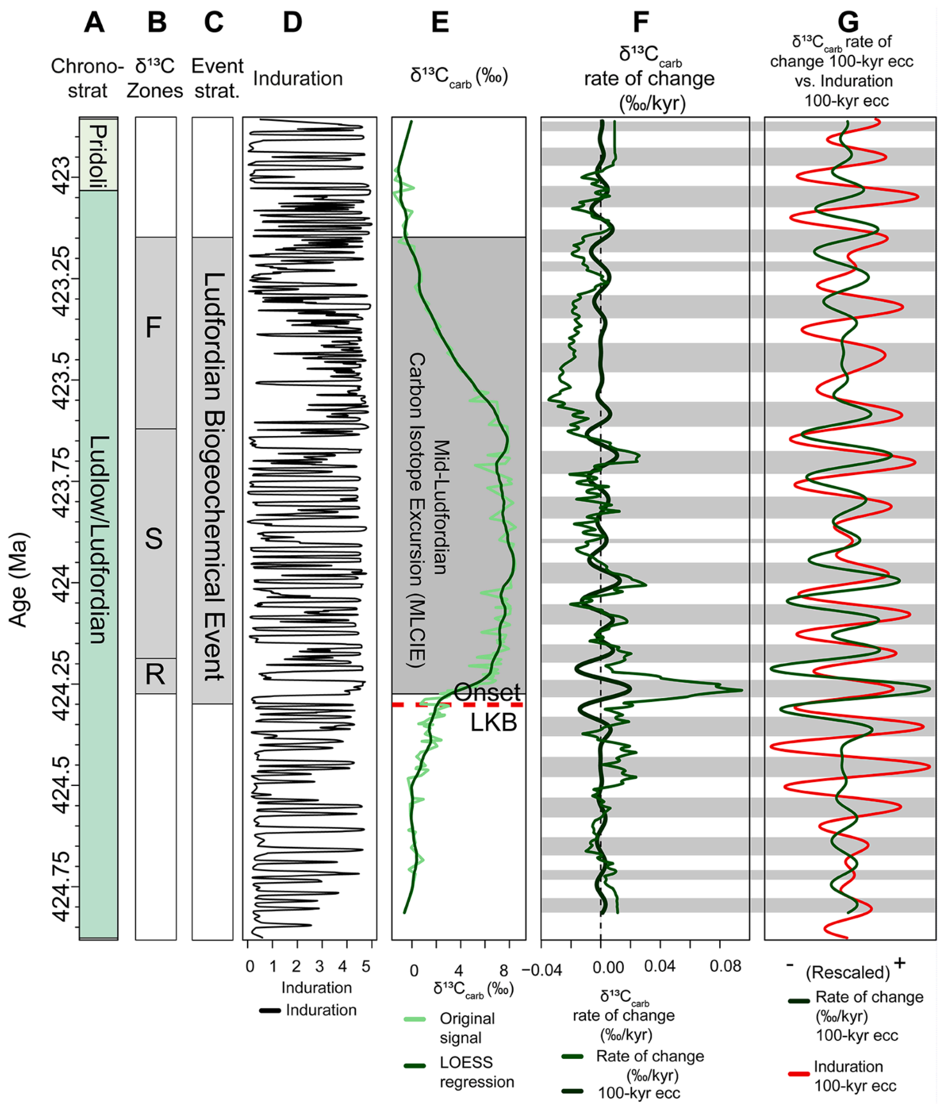

Fig. 8. Rate of change (‰/kyr) of the δ^{13}C$_{carb}$ record. A Stages. B. Isotope zonation. C. Event stratigraphy. D. The Induration record. E. The δ^{13}C$_{carb}$ record (light green), and the LOWESS smoothed curve (dark green) F. The δ^{13}C$_{carb}$ rate of change record (‰/kyr) and the 100-kyr eccentricity cycle extracted from said record. G. The 100-kyr eccentricity cycle extracted from the δ^{13}C$_{carb}$ rate of change record (‰/kyr) (dark green) and the 100-kyr eccentricity cycle extracted from the induration record (red). Grey bars denote maxima in the 100-kyr eccentricity cycle extracted from the induration records which correspond to astronomical 100-kyr eccentricity minima.

scalogram (Fig. 7F). This spectral peak could correspond to the 55-kyr or 54-kyr eccentricity cycle or the 52.8-kyr obliquity cycle (Laskar, 2020; Laskar et al., 2004). The spectral power of the 55-kyr cycle in the CWT scalogram is highly variable, indicating that the 55-kyr cycle might be transient and unrelated to astronomical forcing (Fig. 7F). A 200-kyr cycle can also be identified in the record (Fig. 7F). Given the strong imprint of the 100-kyr and 405-kyr eccentricity cycles, it is reasonable to interpret the 200-kyr cycle as the seldom observed 200-kyr eccentricity cycle (Hilgen et al., 2020).

Several longer-term trends/cycles can be observed in the data, including a spectral peak at 800 kyr (Fig. 7F). The 800-kyr can be linked to the 812-kyr obliquity cycle (Hinnov, 2000). However, since the record is rather short (2020 kyr), there is substantial uncertainty about whether the 800-kyr cycle is truly astronomical in origin or an artefact of underlying long-term trends. The same is true for the impact of the longer cycles, such as the 1.2 Myr obliquity and 2.4 Myr eccentricity cycle, which have been suggested to play a role in pacing Palaeozoic events (Crampton et al., 2018; Sproson, 2020; Sproson et al., 2022). To fully understand the impact of astronomical forcing on the LBE, including the long multi-million-year astronomical cycles, substantially longer records are needed.

5.1.1. Phase relationships and eccentricity driven insolation control on induration

The amplitude modulation of astronomical cycles in the induration record provides an insight into the phase relationships between proxy signals and "true" astronomical cycles (Arts et al., 2024; Hinnov, 2000; Laurin et al., 2017; Zeeden et al., 2015). Since amplitude-modulating cycles affect the signal amplitude in a unidirectional manner, the astronomical cycles extracted from amplitude records are in phase with their true astronomical cycle counterparts, regardless of whether the proxy responds positively or negatively to insolation forcing (Arts et al., 2024; Hinnov, 2000; Laurin et al., 2017; Zeeden et al., 2015)(SI 1). The 100- and 405-kyr eccentricity cycles extracted from the precession and 100-kyr eccentricity amplitude records, respectively, show an anti-phase relationship with the corresponding eccentricity cycles directly extracted from the induration record (Fig. 7G, J). This relationship indicates that minima in the astronomical eccentricity cycles correspond to maxima in the equivalent components extracted from the induration record.

The phase relationship provides a mechanistic explanation of how changes in eccentricity-driven insolation influenced bed hardness. During eccentricity maxima, increased seasonal variability likely enhanced runoff and detrital input, thereby suppressing carbonate production and producing softer, shale- and clay-rich beds with lower induration. Conversely, during eccentricity minima, reduced seasonality favoured carbonate production, generating the harder, more competent limestone beds that allow the induration record to directly reflect

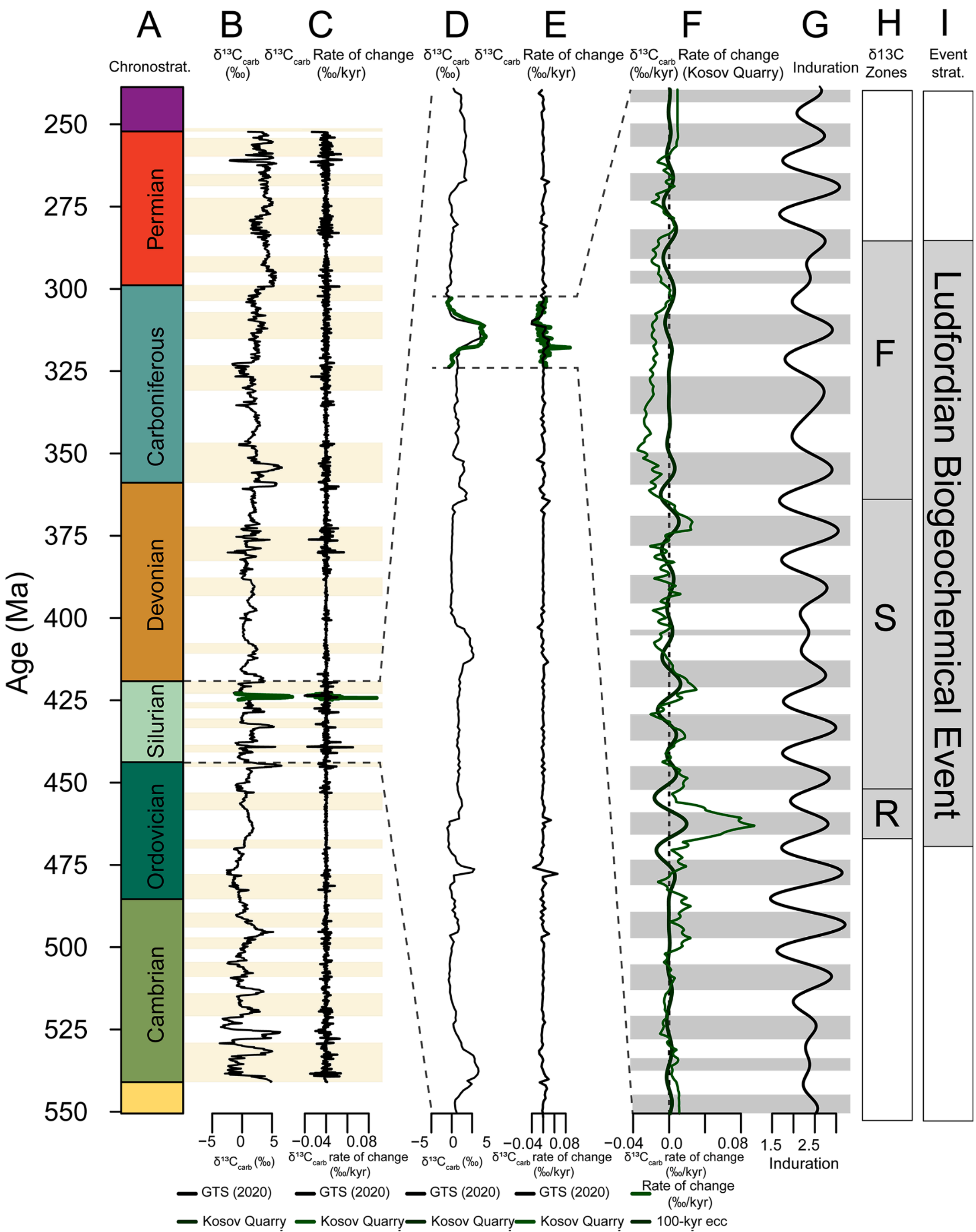

Fig. 9. The GTS 2020 $\delta^{13}C_{carb}$ curve and the $\delta^{13}C_{carb}$ rate of change curve calculated from the $\delta^{13}C_{carb}$ curve, which is compared to the $\delta^{13}C_{carb}$ record and $\delta^{13}C_{carb}$ rate of change record from the Kosov section. A. Timescale GTS 2020 (shifted up by 0.25 Myrs). B. $\delta^{13}C_{carb}$ curve from the GTS 2020 (shifted up by 0.25 Myrs) overlain by the $\delta^{13}C_{carb}$ curve of the Kosov section. C. $\delta^{13}C_{carb}$ rate of change (‰/kyr) curve calculated based on the $\delta^{13}C_{carb}$ curve from the GTS 2020 (shifted up by 0.25 Myrs) overlain by the $\delta^{13}C_{carb}$ rate of change (‰/kyr) curve based on the Kosov section. D. The Silurian $\delta^{13}C_{carb}$ curve from the GTS 2020 (shifted up by 0.25 Myrs) overlain by the $\delta^{13}C_{carb}$ curve of the Kosov section. E. The Silurian $\delta^{13}C_{carb}$ rate of change (‰/kyr) curve, calculated based on the δ13Ccarb curve from the GTS 2020 (shifted up by 0.25 Myrs), overlain by the $\delta^{13}C_{carb}$ rate of change (‰/kyr) curve based of the Kosov section. F. The $\delta^{13}C_{carb}$ rate of change record (‰/kyr) and the 100-kyr eccentricity cycle extracted from said record. G. 100-kyr eccentricity cycle extracted from the induration record. Grey bars denote 100-kyr eccentricity maxima in the induration record, which correspond to astronomical 100-kyr eccentricity minima. H. Isotope zonation. I. Event zonation.

eccentricity-modulated carbonate content (Martinez, 2018; Mutterlose and Ruffell, 1999).

The established relationship between eccentricity and induration can also be used to interpret the imprint of astronomical cycles on the rate of change (‰/kyr) of the $\delta^{13}C_{carb}$ record. Since the 100-kyr eccentricity cycle extracted from the rate of change (‰/kyr) record is generally in phase with the 100-kyr eccentricity cycle extracted from the induration record, it can be inferred that the $\delta^{13}C_{carb}$ rate of change (‰/kyr) is the highest during astronomical eccentricity minima (Fig. 7J).

5.2. Evaluating the drivers and pacing of the carbon-cycle during the Ludfordian Biogeochemical Event

The new astrochronologically anchored age model enables the first robust estimation of $\delta^{13}C_{carb}$ rate-of-change (‰/kyr) values across the LBE (Figs. 8,9). Until now, the tempo of major Palaeozoic carbon isotope excursions has remained poorly constrained. Most studies report $\delta^{13}C_{carb}$ variations as differences across discrete intervals spanning tens to hundreds of kiloyears, so while the overall magnitude and duration of excursions are known, their true rates of change remain unresolved, limiting quantitative comparisons among carbon-cycle perturbations (Maloof et al., 2010; Reershemius and Planavsky, 2021; Ma et al., 2022; De Vleeschouwer et al., 2024; Zhang et al., 2025; Huygh et al., 2026).

By utilising a LOWESS regression of the $\delta^{13}C_{carb}$ curve to minimise short-term noise, we establish a stable regional reference curve that allowed for the calculation of the $\delta^{13}C_{carb}$ rates of change (Fig. 8F). During the LBE, $\delta^{13}C_{carb}$ rate-of-change values reached a maximum of +0.09 ‰/kyr. This is approximately four times higher than the ~0.02 ‰/kyr estimate derived from the GTS 2020 timescale (Cramer and Jarvis, 2020; Gradstein et al., 2020)(Fig. 9C, E, F). These results demonstrate that rate-of-change values depend heavily on the underlying age model, highlighting the importance of cyclostratigraphy for resolving Palaeozoic event dynamics. Ultimately, regardless of the specific model used, the unusually large amplitudes and high rates of change observed underscore the extreme sensitivity of the Silurian carbon cycle (Fig. 9C, E, F).

5.2.1. Astronomical pacing of carbon cycle dynamics

The $\delta^{13}C_{carb}$ rate-of-change record contains a clear imprint of the 100-kyr eccentricity cycle during the R and S isotope zones (Figs. 8F-G, 9F-G). The highest $\delta^{13}C_{carb}$ rates-of-change consistently occur during short astronomical eccentricity minima, suggesting that minima in eccentricity dampened the amplitude of climatic precession, thereby decreasing seasonal contrast and producing more stable climatic conditions. These conditions would have resulted in enhanced burial and preservation of organic carbon in quasi-stable anoxic deep-ocean reservoirs, sensu Sproson (2020) and Sproson et al. (2022).

5.2.2. Drivers of the amplified $\delta^{13}C_{carb}$ rate-of-change signal

Astronomical forcing alone cannot explain the amplified $\delta^{13}C_{carb}$ rate-of-change signal during the R and S isotope zones (Figs. 8F-G, 9F-G). Recent evidence suggests the LBE was initiated by an anomalous influx of trace metals into the ocean, which promoted the expansion of shallow-marine anoxia (Frýda et al., 2021a; De Backer et al., 2026). This period of elevated trace metal concentrations persisted for approximately 350 ± 80 kyr (from 424.6 ± 0.65 Ma to 424.25 ± 0.61 Ma) while the carbon cycle's prolonged volatility during the R and S zones (424.27 ± 0.61 to 423.62 ± 0.56 Ma), continued long after trace-metal concentrations had returned to baseline levels. A secondary amplification mechanism is therefore required to sustain the observed carbon cycle response.

Two distinct frameworks offer plausible secondary amplification pathways via large-scale reorganisation of ocean circulation. The first involves climatic state switching between the so-called P and S ocean-climate states (Jeppsson, 1990; Jeppsson et al., 1995; Bickert et al., 1997; Calner, 2008; Cramer and Saltzman, 2005). During the onset of a Silurian event, a transition from a humid P-state, characterised by enhanced runoff and marl-dominated sedimentation, to an arid S-state with reduced runoff and widespread carbonate production occurs. Such a state switch also entails a fundamental shift toward a negative evaporation-precipitation balance in low-latitude shelfal areas, which would result in the creation of dense, saline surface waters that activate low-latitude downwelling centres. This process would reorganise ocean circulation patterns, promoting water-column stratification and the development of widespread deep-ocean anoxia, creating a quasi-stable deep-ocean carbon reservoir that increases the carbon cycle's sensitivity to external forcing (Sproson, 2020; Sproson et al., 2022).

Alternatively, Earth system modelling by Pohl et al. (2014, 2021, 2022) emphasises high-latitude processes and demonstrates that Palaeozoic ocean circulation was highly sensitive to atmospheric pCO_2. In Hirnantian simulations by Pohl et al. (2021), progressive cooling associated with declining pCO_2 suppresses the formation of high-latitude deep water. The resulting sluggish circulation and decoupling between the shallow, oxygenated and deep, anoxic oceans would have made the deep ocean a quasi-stable carbon reservoir, sensu Sproson (2020) and Sproson et al. (2022). Further cooling in the models of Pohl et al. (2021) shifted deep-water formation to southern high latitudes, increasing ocean ventilation. This scenario closely corresponds to the F isotope zone, during which sea level was low (Manda et al., 2012), $\delta^{13}C_{carb}$ values began to decline, and the rate-of-change of $\delta^{13}C_{carb}$ became negative, reflecting the remineralisation of stored organic carbon and the returning isotopically light carbon to the ocean-atmosphere system (Figs. 8F-G, 9F-G). The absence of strong eccentricity pacing during the F-zone suggests that carbon burial was no longer dominated by eccentricity-paced stagnation. Although rising pCO_2 should have triggered a return to a sluggish circulation regime, hysteresis-like behaviour, in which nonlinear sea-ice and heat-transport feedbacks allowed the climate to follow an alternative recovery branch, could have avoided another episode of deep-ocean anoxia (Pohl et al., 2014). This highlights a key distinction between models: while the Pohl et al. (2021) framework accounts for the systems recovery, the P-to-S state-switch framework currently lacks such a mechanism.

Whether driven by low-latitude downwelling during P-to-S transitions or enhanced high-latitude ventilation under declining pCO_2, vertical decoupling resolves the Silurian paradox of simultaneous carbonate deposition and major positive $\delta^{13}C_{carb}$ excursions. As it explains the transition from marl- and shale-dominated successions to carbonate-rich facies on low-latitude shelves (Aldridge et al., 1993; Cramer and Saltzman, 2007a, 2007b; Jeppsson, 1990; Jeppsson et al., 1995). By invoking oxygenated surface waters above a stratified, poorly ventilated deep ocean, the resulting stable surface conditions fostered reef and platform development, while the isolated deep basins promoted organic carbon burial, driving the $\delta^{13}C_{carb}$ excursion. Astronomical forcing further regulated this system; specifically, reduced seasonality during eccentricity minima stabilised runoff and nutrient delivery, simultaneously promoting shallow-shelf carbonate production and deep-ocean stratification. Consequently, while $\delta^{13}C_{carb}$ rate-of-change values and carbonate deposition co-occur, they are only indirectly linked as concurrent responses to the same astronomical pacing

Although distinguishing between specific circulation models requires expanded multi-proxy datasets, the $\delta^{13}C_{carb}$ record provides critical insight into the timing of these reorganisations. Persistently positive rate-of-change values in the R and S zones indicate sustained net carbon burial (Figs. 8F-G, 9F-G). The absence of the periodic reversals expected from the remineralisation of organic carbon suggests that astronomical forcing did not drive repeated oscillations between circulation states; rather, the system crossed a threshold once at the onset of the LBE.

5.2.3. The LBE as a mechanistic template for interpreting Phanerozoic carbon isotope excursions

Shifts between distinct ocean circulation states provide a mechanistic explanation not only for the LBE but also for other Silurian carbon-cycle perturbations. Relatively modest perturbations to the baseline climate could have pushed the Silurian ocean system past tipping points, reorganising the ocean circulation state. From this perspective, the LBE does not represent an isolated oceanographic anomaly but a latent sensitivity within the Palaeozoic climate system. The similarities between the LBE and the Hirnantian Carbon Isotope Excursion (HICE) as modelled by Pohl et al. (2021) suggest that the boundary conditions enabling the shelf behaviour may already have been established by the Late Ordovician. Hence, the HICE may represent an earlier manifestation of climate instabilities that continued to influence Silurian oceanography, with Silurian events reflecting repeated expressions of the same underlying sensitivity.

As a particularly well-resolved example of Earth system threshold behaviour, the LBE serves as a deep-time benchmark for assessing the sensitivity, pacing, and magnitude of the carbon cycle. The astronomically paced $\delta^{13}C_{carb}$ rate-of-change record (Figs. 8, 9) underscores the importance of incorporating astronomical forcing into future Earth system modelling and stratigraphic studies when investigating carbon-cycle perturbations. Furthermore, concepts such as circulation-mode switching, pCO_2 sensitivity, and the development of an astronomically paced quasi-stable deep ocean carbon reservoirs represent fundamental Earth-system aspects (Duplessy and Shackleton, 1985; Batenburg et al., 2016; Laurin et al., 2017; De Vleeschouwer, 2020; Westerhold, 2020; Martinez et al., 2023; Vervoort et al., 2024, 2026). The LBE can thus also serve as a mechanistic template for interpreting other Phanerozoic $\delta^{13}C$ excursions. In this context, the LBE not only records a Silurian carbon-cycle perturbation but also illustrates how astronomical forcing, when amplified by threshold behaviour, can pace the carbon cycle to a surprisingly large degree.

6. Conclusions

This new astrochronology from the Kosov section provides the first continuous, anchored framework for the Ludfordian Biogeochemical Event (LBE), the largest positive $\delta^{13}C_{carb}$ excursion of the Phanerozoic. Cyclostratigraphic data indicates that the LBE began at 424.30 ± 0.61 Ma and lasted 1150 ± 260 kyr. At the onset of the event, $\delta^{13}C_{carb}$ rate-of-change values reached a maximum of +0.09 ‰/kyr, demonstrating that Silurian carbon-cycle perturbations were not only large in magnitude but also unusually rapid.

Both the induration (the degree of rock hardness) and $\delta^{13}C_{carb}$ rate-of-change records reveal a pervasive imprint of astronomical cycles, ranging from precession to the 405-kyr eccentricity cycle. Phase relationships derived from amplitude modulation indicate that the induration record is anti-phased with astronomical eccentricity cycles, consistent with reduced runoff and enhanced carbonate production during eccentricity minima. Critically, the $\delta^{13}C_{carb}$ rate-of-change record contains a strong 100-kyr eccentricity signal, with maxima occurring during astronomical eccentricity minima. This provides direct evidence of an eccentricity-paced carbon cycle during the Silurian and establishes the $\delta^{13}C_{carb}$ rate of change as a powerful proxy for resolving the tempo of deep-time carbon cycle perturbations.

While astronomical forcing robustly explains the pacing of carbon burial, it does not account for the sustained amplification of $\delta^{13}C_{carb}$ rate-of-change values during the main phase of the LBE. Instead, the data indicate that the carbon cycle crossed a critical threshold early in the event, resulting in a large-scale reorganisation of ocean circulation. Within the P-S state framework, this threshold is associated with the creation of low-latitude downwelling centres. Whereas, in the model of Pohl et al. (2021), the threshold is defined by a specific pCO_2 tipping point that triggers suppression of high-latitude deep-water formation. Whether driven by these low-latitude circulation changes or pCO_2-sensitive shifts in high-latitude deep-water formation, both mechanisms converge on the same outcome: a vertically decoupled ocean featuring oxygenated shallow shelves and a stratified, anoxic deep ocean. In this state, the deep ocean acted as a quasi-stable carbon reservoir, facilitating carbon accumulation and enhancing the system's sensitivity to astronomical forcing.

These findings indicate that large Silurian carbon-isotope excursions resulted from an intrinsically sensitive Earth system capable of crossing circulation thresholds, with the LBE illustrating how astronomical forcing, amplified by internal feedbacks and ocean circulation reorganisation, can pace high-amplitude carbon-cycle variability.

Declaration of generative AI and AI-assisted technologies in the manuscript preparation process

During the preparation of this work, the author(s) used OpenAI ChatGPT, Mistral AI, and Google Gemini with language editing, text restructuring, and basic coding tasks. After using this tool/service, the author(s) reviewed and edited the content needed and take(s) full responsibility for the content of the published article.

Data availability statement

The data and materials supporting the findings of this study are presented in the article and its supplementary materials. The R code, Quarto document, generated HTML file with embedded R code, and all associated datasets and results are publicly available at https://github.com/stratigraphy/Kosov-cyclostrat and or https://zenodo.org/records/19250767/files/curve2time_unc_anchor_res.rds. Further inquiries may be directed to the corresponding author.

CRediT authorship contribution statement

Michiel Arts: Writing – original draft, Visualization, Methodology, Investigation, Formal analysis, Data curation, Conceptualization. **Damien Pas:** Writing – review & editing. **Jiří Frýda:** Writing – review & editing. **Anne-Christine Da Silva:** Writing – review & editing, Writing – original draft, Supervision, Project administration, Funding acquisition.

Declaration of competing interest

The authors declare that they have no known competing financial interests or personal relationships that could have appeared to influence the work reported in this paper.

Acknowledgements

The FNRS-PDR T.0051.19 grant supported MA. DP. acknowledges the Swiss National Science Foundation grant PZ00P2-193520. JF. was supported by the Grant Agency of the Czech Republic (project GA23-06198S to JF. Alexandre Pohl is thanked for providing a three-day practical introduction to Earth system modelling during the summer of 2021. We thank Brad Cramer for his input, which inspired the use of the δ^{13}Ccarb rate of change as a proxy in this work.

Supplementary materials

Supplementary material associated with this article can be found, in the online version, at doi:10.1016/j.epsl.2026.120101.

References

Aldridge, R.J., Jeppsson, L., Dorning, K.J., 1993. Early Silurian oceanic episodes and events. J. Geol. Soc. 150, 501–513. https://doi.org/10.1144/gsjgs.150.3.0501.

Allman, L.J., Bowman, C.N., Frýda, J., Kozik, N.P., Owens, J.D., Young, S.A., 2024. Constraining reducing conditions in the Prague Basin during the Late Silurian Lau/Kozlowskii extinction event. J. Geol. Soc. London. 181. https://doi.org/10.1144/jgs2023-108.

Arts, M., Corradini, C., Pondrelli, M., Pas, D., Da Silva, A.C., 2024. Age and astronomical forcing in the upper Silurian Cellon section (Carnic Alps, Austria) uncovered using

the WaverideR R package. Front. Earth. Sci. (Lausanne) 12, 1–24. https://doi.org/10.3389/feart.2024.1357751.
Arts, M., 2023. WaverideR: extracting signals from wavelet spectra. https://cran.r-project.org/web/packages/WaverideR/index.
Batenburg, S.J., De Vleeschouwer, D., Sprovieri, M., Hilgen, F.J., Gale, A.S., Singer, B.S., Koeberl, C., Coccioni, R., Claeys, P., Montanari, A., 2016. Astronomical control on the timing of oceanic anoxia in the Late Cretaceous. Clim. Past 12 (10), 1995–2009.
Bathurst, R.G.C., 1987. Diagenetically enhanced bedding in argillaceous platform limestones: stratified cementation and selective compaction. Sedimentology 34, 749–778. https://doi.org/10.1111/j.1365-3091.1987.tb00801.x.
Becker, T.R., Marshall, J.E.A., Da Silva, A.C., Agterberg, F.P., Gradstein, F.M., Ogg, J.G., 2020. The Devonian Period, Geologic Time Scale 2020. BV. https://doi.org/10.1016/B978-0-12-824360-2.00022-X.
Berner, R.A., 2004. The Phanerozoic carbon Cycle: CO2 and O2. Oxford University Press. https://doi.org/10.1093/oso/9780195173338.001.0001.
Bickert, T., Pätzold, J., Samtleben, C., Munnecke, A., 1997. Paleoenvironmental changes in the Silurian indicated by stable isotopes in brachiopod shells from Gotland, Sweden. Geochim. Cosmochim. Acta 61, 2717–2730. https://doi.org/10.1016/S0016-7037(97)00136-1.
Boulila, S., de Rafélis, M., Hinnov, L.A., Gardin, S., Galbrun, B., Collin, P.Y., 2010. Orbitally forced climate and sea-level changes in the paleoceanic tethyan domain (marl-limestone alternations, Lower Kimmeridgian, SE France). Palaeogeog. Palaeoclimatol. Palaeoecol. 292, 57–70.
Calner, M., Eriksson, M.J., 2006. Evidence for rapid environmental changes in low latitudes during the Late Silurian Lau Event: the Burgen-1 drillcore, Gotland, Sweden. Geol. Mag. 143, 15–24. https://doi.org/10.1017/S001675680500169X.
Calner, M., 2005. A Late Silurian extinction event and anachronistic period. Geology 33, 305. https://doi.org/10.1130/G21185.1.
Calner, M., 2008. Silurian global events - At the tipping point of climate change. Mass Extinct. 21–57. https://doi.org/10.1007/978-3-540-75916-4_4.
Calvert, S., Pedersen, T., 1982. Organic carbon accumulation and preservation in marine sediments: how important is anoxia? Organic Matter: Productivity, Accumulation, and Preservation in Recent and Ancient Sediments. Columbia University Press, UK, pp. 819–833.
Claussen, A.L., 2024. Benthic response to the strong Silurian climatic fluctuations-implications from Gotland (Sweden). Facies. 70, 14. https://doi.org/10.1007/s10347-024-00686-x.
Cramer, B.D., Jarvis, I., 2020. Chapter 11 - Carbon Isotope Stratigraphy. Carbon Isotope Stratigraphy. Elsevier B.V. https://doi.org/10.1016/B978-0-12-824360-2.00011-5.
Cramer, B.D., Saltzman, M.R., 2005. Sequestration of 12C in the deep ocean during the early Wenlock (Silurian) positive carbon isotope excursion. Palaeogeogr. Palaeoclimatol. Palaeoecol. 219, 333–349. https://doi.org/10.1016/j.palaeo.2005.01.009.
Cramer, B.D., Saltzman, M.R., 2007a. Fluctuations in epeiric sea carbonate production during Silurian positive carbon isotope excursions: a review of proposed paleoceanographic models. Palaeogeogr. Palaeoclimatol. Palaeoecol. 245, 37–45. https://doi.org/10.1016/j.palaeo.2006.02.027.
Cramer, B.D., Saltzman, M.R., 2007b. Early Silurian paired δ13Ccarb and δ13Corg analyses from the Midcontinent of North America: implications for paleoceanography and paleoclimate. Palaeogeogr. Palaeoclimatol. Palaeoecol. 256, 195–203. https://doi.org/10.1016/j.palaeo.2007.02.032.
Cramer, B.D., Schmitz, M.D., Huff, W.D., Bergström, S.M., 2015. High-precision u-pb zircon age constraints on the duration of rapid biogeochemical events during the ludlow epoch (Silurian period). J. Geol. Soc. London. 172, 157–160. https://doi.org/10.1144/jgs2014-094.
Crampton, J .S., Meyers, S.R., Cooper, R.A., Sadler, P.M., Foote, M., Harte, D., 2018. Pacing of Paleozoic macroevolutionary rates by Milankovitch grand cycles. Proc. Natl. Acad. Sci. USA 115 (22), 5686–5691. https://doi.org/10.1073/pnas.1714342115.
De Backer, T., Emsbo, P., McLaughlin, P., Vancoppenolle, I., Klock, C., Munnecke, A., Vandenbroucke, T., 2026. Metal induced chitinozoan malformations link the Mid-Ludfordian OAE to the venting of metalliferous hydrothermal basin brines into the Silurian Ocean. Glob. Planet. Change 259, 105303. https://doi.org/10.1016/j.gloplacha.2026.105303.
De Vleeschouwer, D., Drury, A.J., Vahlenkamp, M., Rochholz, F., Liebrand, D., Pälike, H., 2020. High-latitude biomes and rock weathering mediate climate-carbon cycle feedbacks on eccentricity timescales. Nat. Commun. 11, 5013. https://doi.org/10.1038/s41467-020-18733-w.
De Vleeschouwer, D., Percival, L.M.E., Wichern, N.M.A., Batenburg, S.J., 2024. Pre-Cenozoic cyclostratigraphy and palaeoclimate responses to astronomical forcing. Nat. Rev. Earth Environ. 5, 59–74. https://doi.org/10.1038/s43017-023-00505-x.
del Rey, Á., Frýda, J., Calner, M., Frýdová, B., Zhang, F., Wang, C., Planavsky, N., Dahl, T.W., 2023. Mid-Ludfordian uranium isotope records distinguish the role of expansive marine anoxia in global carbon cycle dynamics during the late Silurian Lau/Kozlowskii bioevent. Glob. Planet. Change. 229, 104248. https://doi.org/10.1016/j.gloplacha.2023.104248.
Duplessy, J.C, Shackleton, N.J., 1985. Response of global deep-water circulation to Earth's climatic change 135,000-107,000 years ago. Nature 316 (6028), 500–507.
Emeis, K.C., Weissert, H., 2009. Tethyan-Mediterranean organic carbon-rich sediments from Mesozoic black shales to sapropels. Sedimentology 56, 247–266. https://doi.org/10.1111/j.1365-3091.2008.01026.x.
Farhat, M., Auclair-Desrotour, P., Boué, G., Laskar, J., 2022. The resonant tidal evolution of the Earth-Moon distance. Astron. Astrophys. 665, L1. https://doi.org/10.1051/0004-6361/202243445.
Farkaš, J., Frýda, J., Holmden, C., 2016. Calcium isotope constraints on the marine carbon cycle and CaCO3 deposition during the late Silurian (Ludfordian) positive δ^{13}C excursion. Earth. Planet. Sci. Lett. 451, 31–40. https://doi.org/10.1016/j.epsl.2016.06.038.
Farkaš, J., Wallmann, K., Mosley, L., Staudigel, P., Zheng, X.-Y., Leyden, E., Shao, Y., Frýda, J., Holmden, C., Eisenhauer, A., 2024. Alkalinity and elemental cycles in present and past ocean: insight from Geochemical Modeling and Alkali and Alkaline Earth Metal Isotopes. Reference Module in Earth Systems and Environmental Sciences. Treatise on Geochemistry 5. Elsevier, Rotterdam, pp. 33–87. https://doi.org/10.1016/B9780323997621.000371b.
Frýda, J., Manda, Š., 2013. A long-lasting steady period of isotopically heavy carbon in the late Silurian ocean: evolution of the delta;13 record and its significance for an integrated delta;13, graptolite and conodont stratigraphy. Bull. Geosci. 463–482. https://doi.org/10.3140/bull.geosci.1436.
Frýda, J., Lehnert, O., Frýdová, B., Farkaš, J., Kubajko, M., 2021a. Carbon and sulfur cycling during the mid-Ludfordian anomaly and the linkage with the late Silurian Lau/Kozlowskii Bioevent. Palaeogeogr. Palaeoclimatol. Palaeoecol. 564, 110152. https://doi.org/10.1016/j.palaeo.2020.110152.
Frýda, J., Lehnert, O., Joachimski, M.M., Männik, P., Kubajko, M., Mergl, M., Farkaš, J., Frýdová, B., 2021b. The Mid-Ludfordian (late Silurian) Glaciation: a link with global changes in ocean chemistry and ecosystem overturns. Earth. Sci. Rev. 220, 103652. https://doi.org/10.1016/j.earscirev.2021.103652.
Gambacorta, G., Bersezio, R., Weissert, H., Erba, E., 2016. Onset and demise of Cretaceous oceanic anoxic events: the coupling of surface and bottom oceanic processes in two pelagic basins of the western Tethys. Paleoceanography 31, 732–757. https://doi.org/10.1002/2015PA002922.
Gocke, M., Lehnert, O., Frýda, J., 2013. Facies development across the Late Silurian Lau Event based on temperate carbonates of the Prague Basin (Czech Republic). Facies 59, 611–630. https://doi.org/10.1007/s10347-012-0328-y.
Gradstein, F.M., Ogg, J.G., Schmitz, M.D., Ogg, G.M., 2020. Chapter 14 - geomathematics. Geologic Time Scale 2020, pp. 401–439. https://doi.org/10.1016/B978-0-12-824360-2.00014-0 (eds).
Gregory, J.M., Jones, C.D., Cadule, P., Friedlingstein, P., 2009. Quantifying carbon cycle feedbacks. J. Clim. 22, 5232–5250. https://doi.org/10.1175/2009JCLI2949.1.
Hays, J.D.D., Imbrie, J.Z., Shackleton, N.J., 1976. Variations in the earth's orbit: pacemaker of the ice ages. Science (1979) 194, 1121–1132. https://doi.org/10.1126/science.194.4270.1121.
Hilgen, F., Zeeden, C., Laskar, J., 2020. Paleoclimate records reveal elusive 200-kyr eccentricity cycle for the first time. Glob. Planet. Change 194, 103296. https://doi.org/10.1016/j.gloplacha.2020.103296.
Hinnov, L.A., Hilgen, F.J., 2012. Cyclostratigraphy and astrochronology. The Geologic Time Scale 2012, pp. 63–83. https://doi.org/10.1016/B978-0-444-59425-9.00004-4.
Hinnov, L.A., 2004. New perspectives on astronomically forced stratigraphy. Annu Rev. Earth. Planet. Sci. 55, 5–22. https://doi.org/10.1177/0741713604268894.
Hinnov, L.A., 2013. Cyclostratigraphy and its revolutionizing applications in the earth and planetary sciences. Bull. Geol. Soc. Am. 125, 1703–1734. https://doi.org/10.1130/B30934.1.
Hinnov, L.A., 2018. Cyclostratigraphy and Astrochronology in 2018. Stratigraphy & Timescales. Elsevier Ltd. https://doi.org/10.1016/bs.sats.2018.08.004.
Horný, R., 1955. Base vrstev kopaninských eß 1 na jihozápadním okraji vulkanické facie (Kosov u Berouna). Věstník Ústředního ústavu geologického 30, 81–86.
Huang, H., Gao, Y., Ma, C., Jones, M.M., Zeeden, C., Ibarra, D.E., Wu, H., Wang, C., 2021. Organic carbon burial is paced by a ~173-ka obliquity cycle in the middle to high latitudes. Sci. Adv. 7, 1–11. https://doi.org/10.1126/sciadv.abf9489.
Huygh, J.J., Algeo, T.J., Sageman, B.B., Arts, M., Ver Straeten, C.A., Over, D.J., Gérard, J., Sablon, L., Crucifix, M., Da Silva, A.C., 2026. Astronomical control on marine anoxia during the Kellwasser Crisis and Rhinestreet Event (Appalachian Basin, New York, USA). Glob. Planet. Change 257, 105216. https://doi.org/10.1016/j.gloplacha.2025.105216.
Isson, T.T., Planavsky, N.J., Coogan, L.A., Stewart, E.M., Ague, J.J., Bolton, E.W., Zhang, S., McKenzie, N.R., Kump, L.R., 2020. Evolution of the global carbon cycle and climate regulation on earth. Global. Biogeochem. Cycles. 34. https://doi.org/10.1029/2018GB006061.
Jeppsson, L., Aldridge, R.J., Dorning, K.J., 1995. Wenlock (Silurian) oceanic episodes and events. J. Geol. Soc. 152, 487–498. https://doi.org/10.1144/gsjgs.152.3.0487.
Jeppsson, L., 1990. An oceanic model for lithological and faunal changes tested on the Silurian record. J. Geol. Soc. London. 147, 663–674. https://doi.org/10.1144/gsjgs.147.4.0663.
Kříž, J., 1991. The Silurian of the Prague Basin (Bohemia)-tectonic, eustatic and volcanic controls on facies and faunal development. Spec. Pap. Palaeontol. 44, 179–203.
Kříž, J., 1992. Silurian Field Excursions: Prague Basin (Barrandian). National Museum of Wales, Bohemia.
Kozłowski, W., Sobień, K., 2012. Mid-Ludfordian coeval carbon isotope, natural gamma ray and magnetic susceptibility excursions in the Mielnik IG-1 borehole (Eastern Poland)-Dustiness as a possible link between global climate and the Silurian carbon isotope record. Palaeogeogr. Palaeoclimatol. Palaeoecol. 339-341, 74–97. https://doi.org/10.1016/j.palaeo.2012.04.024.
Laskar, J., Robutel, P., Joutel, F., Gastineau, M., Correia, A.C.M., Levrard, B., 2004. A long-term numerical solution for the insolation quantities of the Earth. Astron. Astrophys. 428, 261–285. https://doi.org/10.1051/0004-6361:20041335.
Laskar, J., Fienga, A., Gastineau, M., Manche, H., 2011. La2010: A new orbital solution for the long-term motion of the Earth. Astron. Astrophys. 532, 15.
Laskar, J., 2020. Astrochronology. Geologic Time Scale 2020. Elsevier, pp. 139–158. https://doi.org/10.1016/B978-0-12-824360-2.00004-8.
Laurin, J., Meyers, S.R., Uličný, D., Jarvis, I., Sageman, B.B, 2015. Axial obliquity control on the greenhouse carbon budget through middle- to high-latitude reservoirs. Paleoceanography 30, 133–149. https://doi.org/10.1002/2014PA002736.

Laurin, J., Růžek, B., Giorgioni, M., 2017. Astronomical signals in carbon isotopes: phase distortion as a signature of the carbon cycle. Paleoceanography 32, 1236–1255. https://doi.org/10.1002/2017PA003143.

Lehnert, O., Frýda, J., Buggisch, W., Munnecke, A., Nützel, A., Křiž, J., Manda, S., 2007a. δ^{13}C records across the late Silurian Lau event: new data from middle palaeo-latitudes of northern peri-Gondwana (Prague Basin, Czech Republic). Palaeogeogr. Palaeoclimatol. Palaeoecol. 245, 227–244. https://doi.org/10.1016/j.palaeo.2006.02.022.

Lehnert, O., Eriksson, M.E., Calner, M., Joachimski, M., Buggisch, W., 2007b. Concurrent sedimentary and isotopic indications for global climatic cooling in the Late Silurian. Acta Palaeontol. Sin. 46, 249–255.

Li, Z.H., Guo, Z., Chen, Z.Q., Poulton, S.W., Bao, Y., Zhao, L., Zhang, F.F., 2021. A novel carbon cycle turbulence index identifies environmental and ecological perturbations. Geochem. Perspect. Lett. 20, 11–15. https://doi.org/10.7185/geochemlet.2137.

Ma, W., Tian, J., Li, Q., Wang, P., 2011. Simulation of long eccentricity (400-kyr) cycle in ocean carbon reservoir during miocene climate optimum: weathering and nutrient response to astronomical change. Geophys. Res. Lett. 38, n/a-n/a. https://doi.org/10.1029/2011GL047680.

Ma, X., Ogg, J., Lu, Y., Fan, R., Huang, C., Luo, Z., Deng, S., 2022. The upper ordovician Pagoda positive δ13C excursion (PPCE) on the upper Yangtze platform, South China. J. Asian Earth. Sci. 240, 105373. https://doi.org/10.1016/j.jseaes.2022.105373.

Maloof, A.C., Ramezani, J., Bowring, S.A., Fike, D.A., Porter, S.M., Mazouad, M., 2010. Constraints on early Cambrian carbon cycling from the duration of the Nemakit-Daldynian–Tommotian boundary δ13C shift, Morocco. Geology. 38 (7), 623–626. https://doi.org/10.1130/G30726.1.

Manda, Š., Kříž, J., 2006. Environmental and biotic changes in subtropical isolated carbonate platforms during the Late Silurian Kozlowskii Event, Prague Basin. GFF 128, 161–168. https://doi.org/10.1080/11035890601282161.

Manda, Š., Štorch, P., Slavik, L., Frýda, J., Kříž, J., Tasaryova, Z., 2012. The graptolite, conodont and sedimentary record through the late Ludlow Kozlowskii Event (Silurian) in the shale-dominated succession of Bohemia. Geol. Mag. 149 (3), 507–531.

Marsaglia, K.M., Browne, G.H., George, S.C., Kemp, D.B., Jaeger, J.M., Carson, D., Richaud, M., IODP Expedition 317 Scientific Party, 2017. The Transformation of sediment into rock: insights from IODP site U1352, Canterbury Basin, New Zealand. J. Sediment. Res. 87, 272–287. https://doi.org/10.2110/jsr.2017.15.

Martinez, M., Aguirre-Urreta, B., Dera, G., Lescano, M., Omarini, J., Tunik, M., O'Dogherty, L., Aguado, R., Company, M., and Bodin, S., 2023, Synchrony of carbon cycle fluctuations, volcanism and astronomical forcing during the early cretaceous: Earth-science reviews, v. 239, doi:10.1016/j.earscirev.2023.104356.

Martinez, M., 2018. Mechanisms of preservation of the eccentricity and longer-term Milankovitch cycles in detrital supply and carbonate production in Hemipelagic Marl-limestone alternations. Stratigraphy & Timescales. Elsevier Ltd. https://doi.org/10.1016/bs.sats.2018.08.002.

Melchin, M.J., Sadler, P.M., Cramer, B.D., 2020. The Silurian Period, Geologic Time Scale 2020. BV. https://doi.org/10.1016/B978-0-12-824360-2.00021-8.

Mergl, M., Frýda, J., 2025. Late Silurian brachiopods Dayia and Shaleria as indicators of environmental changes during the 'Lau/Kozlowskii Bioevent' on both sides of the Rheic Ocean. Bull. Geosci. 100 (4), 685–738. https://doi.org/10.3140/bull.geosci.1952.

Meyers, S.R., 2015. The evaluation of eccentricity-related amplitude modulation and bundling in paleoclimate data: an inverse approach for astrochronologic testing and time scale optimization. Paleoceanography 30, 1625–1640. https://doi.org/10.1002/2015PA002850.

Meyers, S.R., 2019. Cyclostratigraphy and the problem of astrochronologic testing. Earth. Sci. Rev. 190, 190–223. https://doi.org/10.1016/j.earscirev.2018.11.015.

Munnecke, A., Samtleben, C., Bickert, T., 2003. The Ireviken Event in the lower Silurian of Gotland, Sweden - Relation to similar Palaeozoic and Proterozoic events. Palaeogeogr. Palaeoclimatol. Palaeoecol. 195, 99–124. https://doi.org/10.1016/S0031-0182(03)00304-3.

Munnecke, A., Calner, M., Harper, D.A.T., Servais, T., 2010. Ordovician and Silurian sea - water chemistry, sea level, and climate: a synopsis. Palaeogeogr. Palaeoclimatol. Palaeoecol. 296, 389–413. https://doi.org/10.1016/j.palaeo.2010.08.001.

Munnecke, A., Wright, V.P., Nohl, T., 2023. The origins and transformation of carbonate mud during early marine burial diagenesis and the fate of aragonite: a stratigraphic sedimentological perspective. Earth. Sci. Rev. 239, 104366. https://doi.org/10.1016/j.earscirev.2023.104366.

Mutterlose, J., Ruffell, A., 1999. Milankovitch-scale palaeoclimate changes in pale-dark bedding rhythms from the Early Cretaceous (Hauterivian and Barremian) of eastern England and northern Germany. Palaeogeogr. Palaeoclimatol. Palaeoecol. 154, 133–160. https://doi.org/10.1016/S0031-0182(99)00107-8.

Ohkouchi, N., Kuroda, J., Taira, A., 2015. The origin of Cretaceous black shales: a change in the surface ocean ecosystem and its triggers. Proc. Jpn. Acad. Ser. B Phys. Biol. Sci. 91, 273–291. https://doi.org/10.2183/pjab.91.273.

Pas, D., Elrick, M., Da Silva, A.C., Hinnov, L., Jamart, V., Thaureau, M., Arts, M., 2024. Millennial-scale climate cycles modulated by Milankovitch forcing in the middle Cambrian (ca. 500 Ma) Marjum Formation, Utah, USA. Geology 52, 605–609. https://doi.org/10.1130/G52182.1.

Pohl, A., Donnadieu, Y., Hir, G., Buoncristiani, J-F., Vennin, E., 2014. Effect of the Ordovician paleogeography on the (in)stability of the climate. Clim. Past 10, 2053–2066. https://doi.org/10.5194/cp-10-2053-2014.

Pohl, A., Lu, Z., Lu, W., Stockey, R.G., Elrick, M., Li, M., Desrochers, A., Shen, Y., He, R., Finnegan, S., Ridgwell, A., 2021. Vertical decoupling in Late Ordovician anoxia due to reorganization of ocean circulation. Nat. Geosci. 14, 868–873. https://doi.org/10.1038/s41561-021-00843-9.

Pohl, A., Ridgwell, A., Stockey, R.G., Thomazo, C., Keane, A., Vennin, E., Scotese, C.R., 2022. Continental configuration controls ocean oxygenation during the Phanerozoic. NatureNature 608, 523–527. https://doi.org/10.1038/s41586-022-05018-z.

Reershemius, T., Planavsky, N.J., 2021. What controls the duration and intensity of ocean anoxic events in the Paleozoic and the Mesozoic? Earth. Sci. Rev. 221, 103787. https://doi.org/10.1016/j.earscirev.2021.103787.

Roberts, J., Turchyn, A.V., Wignall, P.B., Newton, R.J., Vane, C.H., 2018. Disentangling Diagenesis from the rock record: an example from the Permo-Triassic Wordie Creek Formation, East Greenland. Geochem. Geophys. Geosyst. 19, 99–113. https://doi.org/10.1002/2017GC007259.

Saltzman, M.R., 2005. Phosphorus, nitrogen, and the redox evolution of the Paleozoic oceans. Geology. 33, 573. https://doi.org/10.1130/G21535.1.

Scotese, C.R., 2021. An atlas of phanerozoic paleogeographic maps: the seas come in and the seas go out. Annu Rev. Earth. Planet. Sci. 49, 679–728. https://doi.org/10.1146/annurev-earth-081320-064052.

Sproson, A.D., Pogge von Strandmann, P.A.E., Selby, D., Jarochowska, E., Frýda, J., Hladil, J., Loydell, D.K., Slavík, L., Calner, M., Maier, G., Munnecke, A., Lenton, T. M., 2022. Osmium and lithium isotope evidence for weathering feedbacks linked to astronomically paced organic carbon burial and Silurian glaciations. Earth. Planet. Sci. Lett. 577, 117260. https://doi.org/10.1016/j.epsl.2021.117260.

Sproson, A.D., 2020. Pacing of the latest Ordovician and Silurian carbon cycle by a 4.5 Myr astronomical cycle. Palaeogeogr. Palaeoclimatol. Palaeoecol. 540, 109543. https://doi.org/10.1016/j.palaeo.2019.109543.

Štorch, P., 1995. Biotic crises and post-crisis recoveries recorded by Silurian planktonic graptolite faunas of the Barrandian area (Czech Republic). Geolines 3, 59–70.

Tasáryová, Z., Schnabl, P., Čížková, K., Pruner, P., Janoušek, V., Rapprich, V., Štorch, P., Manda, Š., Frýda, J., Trubač, J., 2014. Gorstian palaeoposition and geotectonic setting of Suchomasty Volcanic Centre (Silurian, Prague Basin, Teplá-Barrandian Unit, Bohemian Massif). Gff 136, 262–265. https://doi.org/10.1080/11035897.2013.879735.

Tonarová, P., Frýda, J., Kubajko, M., Hints, O., 2025. Response of the jawed polychaete fauna to the mid-Ludfordian (late Silurian) carbon isotope excursion and associated extinction events in the Prague Basin (Czech Republic). Bull. Geosci. 100 (4), 617–644. https://doi.org/10.3140/bull.geosci.1913.

Trotter, J.A., Williams, I.S., Barnes, C.R., Männik, P., Simpson, A.J., 2016. New conodont δ^{18}O records of Silurian climate change: implications for environmental and biological events. Palaeogeogr. Palaeoclimatol. Palaeoecol. 443, 34–48. https://doi.org/10.1016/j.palaeo.2015.11.011.

Vervoort, P., Turner, S.K., Rochholz, F., Ridgwell, A., 2024. Earth system model analysis of how astronomical forcing is imprinted onto the marine geological record: the role of the inorganic (carbonate) carbon cycle and feedbacks. Paleoceanogr. Paleoclimatol. 39. https://doi.org/10.1029/2023PA004826.

Vervoort, P., Kirtland Turner, S., Hülse, D., Greene, S.E., Ridgwell, A., 2026. Earth system model analysis of how astronomical forcing is imprinted onto the marine geological record: the role of the marine organic carbon cycle and feedbacks. Paleoceanogr. Paleoclimatol. 41, e2025PA005181. https://doi.org/10.1029/2025PA005181.

Waltham, D., 2015. Milankovitch Period Uncertainties and Their Impact on Cyclostratigraphy. J. Sediment. Res. 85, 990–998. https://doi.org/10.2110/jsr.2015.66.

Weedon, G.P., 2003. Time-series analysis and cyclostratigraphy: examining stratigraphic records of environmental cycles. Cambridge University Press.

Westerhold, T., Marwan, N., Drury, A.J., Liebrand, D., Agnini, C., Anagnostou, E., Barnet, J.S., Bohaty, S.M., De Vleeschouwer, D., Florindo, F., Frederichs, T., 2020. An astronomically dated record of Earth's climate and its predictability over the last 66 million years. Science (1979) 369 (6509), 1383–1387. https://doi.org/10.1126/science.aba6853.

Westphal, H., 2006. Limestone-marl alternations as environmental archives and the role of early diagenesis - a critical review. Int. J. Earth Sci. 95, 947–961. https://doi.org/10.1007/s00531-006-0084-8.

Wu, Y., Malinverno, A., Meyers, S.R., Hinnov, L.A., 2024. A 650-Myr history of Earth's axial precession frequency and the evolution of the Earth-Moon system derived from cyclostratigraphy. Sci. Adv. 10, eado2412. https://doi.org/10.1126/sciadv.ado2412.

Zeebe, R.E., Ridgwell, A., 2011. Past Changes in Ocean Carbonate Chemistry, in: Ocean Acidification. Oxford University Press. https://doi.org/10.1093/oso/9780199591091.003.0007.

Zeeden, C., Meyers, S.R., Lourens, L.J., Hilgen, F.J., 2015. Testing astronomically tuned age models. Paleoceanography 30, 369–383. https://doi.org/10.1002/2014PA002762.

Zhang, F., Frýda, J., Mojtaba, F., Yi-bo, L., Guangyi, W., Mengchun, C., Na, L., Jianlin, Z., Frýdová, B., Haizhen, W., Shuzhong, S., 2022. Marine anoxia as a trigger for the largest Phanerozoic positive carbon isotope excursion: evidence from carbonate barium isotope records. Earth Planet. Sci. Lett. 584, 117421. https://doi.org/10.1016/j.epsl.2022.117421.

Zhang, Z., Yang, C., Sahy, D., Zhan, R.B., Wu, R.C., Li, Y., Deng, Y., Huang, B., Condon, D. J., Rong, J., Li, X.H., 2025. Tempo of the Late Ordovician mass extinction controlled by the rate of climate change. Sci. Adv. 11 (22), eadv6788. https://doi.org/10.1126/sciadv.adv6788.